Manuscript accepted for publication in Nature Geoscience on 26 June 2020

Back-propagating super-shear rupture in the 2016 M_w 7.1 Romanche transform fault earthquake

Stephen P. Hicks[1,2], Ryo Okuwaki[3,4], Andreas Steinberg[5,6], Catherine A. Rychert[2], Nicholas Harmon[2], Rachel E. Abercrombie[7], Petros Bogiatzis[2], David Schlaphorst[8,9], Jiri Zahradnik[10], J-Michael Kendall[8,11], Yuji Yagi[3], Kousuke Shimizu[3], Henriette Sudhaus[5].

1. Department of Earth Science and Engineering, Imperial College London, United Kingdom.
2. Department of Ocean and Earth Science, University of Southampton, United Kingdom.
3. Mountain Science Center, Faculty of Life and Environmental Sciences, University of Tsukuba, Tsukuba, Japan.
4. COMET, School of Earth and Environment, University of Leeds, Leeds, UK.
5. Department of Geosciences, Christian-Albrechts-Universität, Kiel, Germany
6. BGR, Federal Institute for Geosciences and Natural Resources
7. Department of Earth and Environment, Boston University, United States
8. Department of Earth Science, University of Bristol, United Kingdom.
9. Instituto Dom Luiz (IDL), Faculdade de Ciências, Universidade de Lisboa, Lisbon, Portugal
10. Faculty of Mathematics and Physics, Charles University in Prague, Czech Republic.
11. Department of Earth Sciences, University of Oxford, United Kingdom.

Abstract

How an earthquake rupture propagates strongly influences potentially destructive ground shaking. Complex ruptures often involve slip along multiple faults, which masks information on the frictional behaviour of fault zones. Geometrically smooth ocean transform fault plate boundaries offer a favourable environment to study fault dynamics, because strain is accommodated along a single, wide fault zone that offsets the homogeneous geology. Here we present an analysis of the 2016 M_w 7.1 earthquake on the Romanche fracture zone in the equatorial Atlantic, using data from both nearby seafloor seismometers and global seismic networks. We show that this rupture had two phases: (1) upward and eastward propagation towards a weaker region where the transform fault intersects the mid-ocean ridge, and then (2) an unusual back-propagation westwards at super-shear speed toward the centre of the fault. We suggest that deep rupture into weak fault segments facilitated greater seismic slip on shallow locked zones. This highlights that even earthquakes along a single distinct fault zone can be highly dynamic. Observations of back-propagating ruptures are sparse, and the possibility of reverse propagation is largely absent in rupture simulations and unaccounted for in hazard assessments.

For large earthquakes, many complex configurations of seismic slip have been proposed, such as cascading rupture across multiple faults[1], including for intraplate ocean earthquakes[2], and closely-spaced doublets[3]. These configurations, however, are often dominated by pre-existing complex geometries of multiple faults[4]. In contrast, ocean transform faults (OTFs), which make up ~20% of the total length of global plate boundaries, have most strain accommodated along a single broad zone, a thermally controlled seismogenic width, and well-defined ridge-controlled slip rates, making them the simplest manifestation of transform faults on Earth. OTF faults are strongly bi-material, controlled by plate age variation across the fault, with hydrothermal alteration of mafic and ultramafic rocks[5]. Rupture behaviour along OTFs was thought to be influenced by strongly-coupled, velocity-weakening fault patches[6–8], with short recurrence times of moderate-sized earthquakes (M_w≤6.2) along faster-slipping OTFs in the Pacific[9], allowing for possible earthquake forecasting[9–11]. The wide fault damage zone along OTFs (~5–20 km)[12,13] likely affects seismogenic behaviour[8,14]. These concepts, however, have yet to be explored for larger ruptures along OTFs that offset slower-spreading, Atlantic-type ridges.

Using teleseismic data alone, past studies of OTF earthquakes suggested anomalously long rupture durations[15], with unilateral propagation after initiation closer to the ridge-transform intersection (RTI), then propagating toward the centre of the fault[16–18]. Although fast strike-slip earthquakes are found in continental[19], ocean-continent[20], and oceanic intraplate[2] settings, it remains unclear as to whether OTFs can host super-shear rupture. Fast ruptures might occur given the maturity[21], length, and linearity[22] of OTFs. Whilst OTFs offer a unique opportunity to investigate geological controls on rupture style and seismic cycle behaviour[14], there has been no documented capture and analysis of large earthquakes along OTFs using nearby (i.e. <1,000 km) seafloor sensors.

Uniquely, in August 2016, an M_w 7.1 earthquake at the eastern end of the Romanche OTF in the central Atlantic Ocean was captured by a local ocean-bottom seismometer (OBS) network (**Figure 1**). The 920 km-long Romanche OTF is the second longest globally, and large earthquakes along it are common, with 13 M_w 6.5+ events since 1970, including an M_w 7.1 rupture in 1994[16]. Using local OBS and teleseismic data of the earthquake and its aftershocks, we show that the 2016 earthquake ruptured at super-shear speed with back-propagating fronts along a single fault zone.

Rupture complexity from seafloor and teleseismic waveforms

The mainshock epicentre coincides with the 20-km wide Romanche axial valley, lying ~90 km WSW of the RTI (**Figure 1, Figure 2a**). The hypocentre depth is approximately 20 km below sea level (BSL), although this is poorly constrained due to network coverage (see **Methods**). The magnitude of the largest aftershock is M_L 4.8, consistent with the maximum aftershock magnitude decrement for OTF earthquakes globally of 2.2[5]. We find a high density of aftershocks (see **Methods**) ~20 km west of the mainshock epicentre, and some further east, up to 70 km away (**Figure 2a**). The aftershock distribution relative to the mainshock indicates a ~60-80 km-long bilateral rupture. Regional moment tensor (RMT) analysis (see **Methods**) using a single point-source approximation shows strongly double-couple (98%) right-lateral strike-slip faulting (**Figure 1**). The hypocentre-to-centroid time and epicentre shifts of 16 s and <20 km, respectively imply a slow[15] rupture velocity, $v_r \approx 1$ km/s.

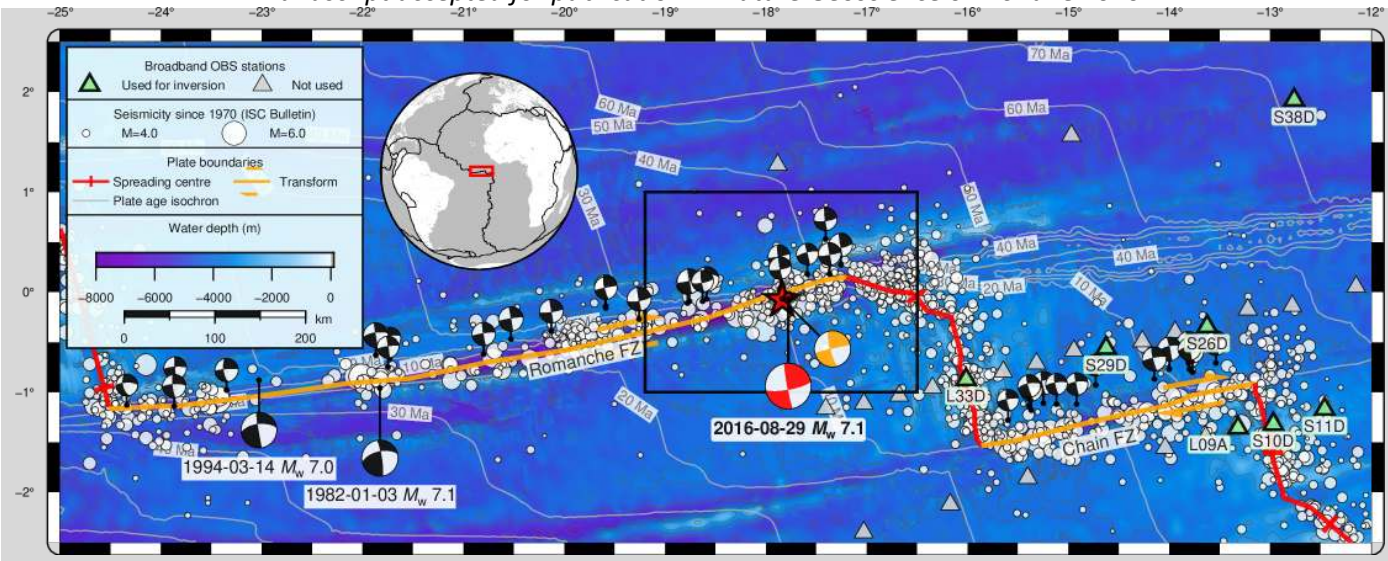

Figure 1: Seismo-tectonic context. Map location is given by the red rectangle on the inset. Focal mechanisms are shown for M_w>6 events[30]. M_w>7.0 events are labelled. Stations of the PI-LAB ocean bottom seismometer network are indicated by triangles. Our relocated hypocentre and low-frequency RMT of the 2016 earthquake are shown by the red star and red beach ball, respectively. The orange beach ball is a co-located M_w 5.8 used for Mach cone analysis. The black rectangle shows the location of map in **Figure 2**.

To investigate this apparently slow rupture, we inverted waveforms at shorter periods to solve for multiple sub-events with variable deviatoric RMTs[23] (see **Methods**). Waveform fits and source configurations are shown in **Figure 2b** and described below. The largest pulse in waveforms is reproduced by an M_w 6.9 sub-event at $\Delta t = 21$ s located close to the epicentre. In the residual waveforms, we fit an earlier pulse with an additional sub-event, which increases overall variance reduction by 20%, statistically significant at 95% confidence (**Note S4**). This M_w 6.7 sub-event ruptured earlier ($\Delta t = 13$ s) than the larger sub-event, with its centroid ~40 km east of the epicentre. We refer to the earlier, smaller sub-event as *SE1* and the later, larger sub-event as *SE2*. In contrast to early indications of a slow unilateral rupture, the location and timing of sub-events indicate a faster, more complex rupture. The resulting source-time function is similar to that from automated teleseismic analyses[24] (**Figure 2c**).

To verify our source model, we inverted teleseismic waveforms for a slip-rate model[25] of the Romanche earthquake (see **Methods**). This model requires a sub-vertical, south-dipping fault plane (~78° dip) with deep initiation, consistent with our RMTs and hypocentre estimate, respectively. The rupture evolution over time (**Figure 3a**) shows a low slip-rate (<2 cm/s) early on ($\Delta t = 0$–8 s), similar to other large OTF earthquakes[16]. At $\Delta t = 8$–14 s, an emergent phase of slip (4 cm/s) occurs ~35 km east of the hypocentre at shallow depth (SE1). Soon after, at $\Delta t > 16$ s, the rupture appears to travel west, toward, and beyond, the nucleation region - rupturing a large asperity ~50 km long in the crust (SE2) with high slip-rate (7 cm/s).

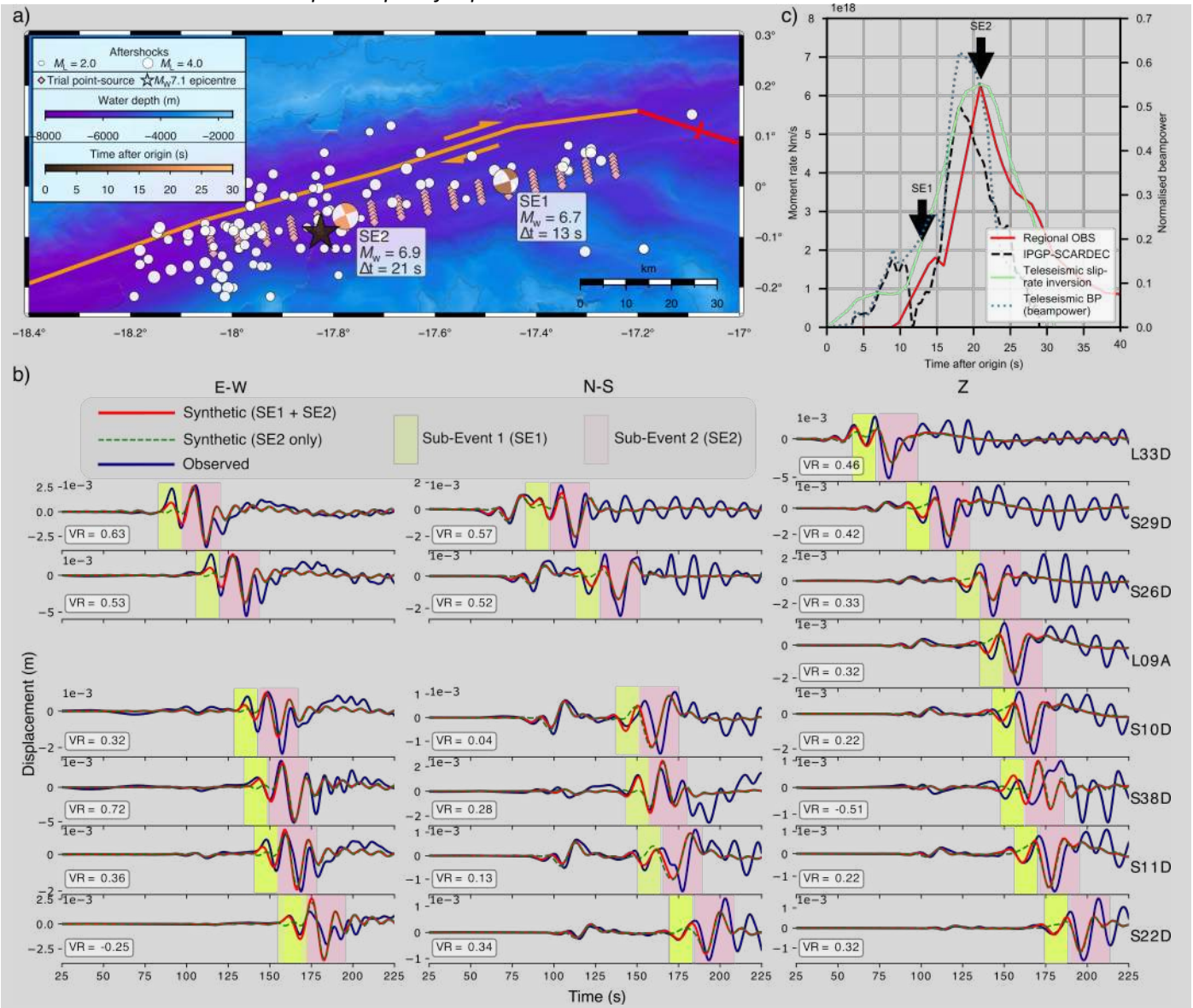

Figure 2: Multiple-point source CMT inversion using OBS waveforms. a) Hypocentral area map of the 2016 Romanche earthquake showing aftershock epicentres and sub-event RMTs coloured by centroid time. b) Waveform fits: displacement waveforms bandpass filtered between 0.01 and 0.1 Hz for multi-point source CMT inversion; shading shows the two sub-event pulses. Synthetics using SE2 are also shown. Waveform variance reduction (VR) is shown in the bottom-left of each panel. Horizontal components for L33D and L09A were removed due to clipping or non-linear tilt effects. c) Total moment-rate functions for different methodologies compared with sub-event centroid times.

Verification of rupture reversal

The aftershock distribution, sub-event RMTs, and teleseismic slip inversion appear consistent, implying two rupture phases propagating in opposite directions. Two models can explain this: either bilateral rupture with vastly different v_r in each direction; or sequential back-propagating rupture with super-shear v_r.

Bilateral super- and sub-shear ruptures were inferred for the 2013 M_w 7.5 Craig, Alaska earthquake[20]. If we assume a similar configuration for the Romanche earthquake, failure of the larger failed asperity (SE2) must have propagated very slowly ($v_r \approx 1$ km/s), requiring, for example, a dissipative mechanism in ductile mantle[26]; however, the earthquake ruptured above the 600°C isotherm (**Figure 4**).

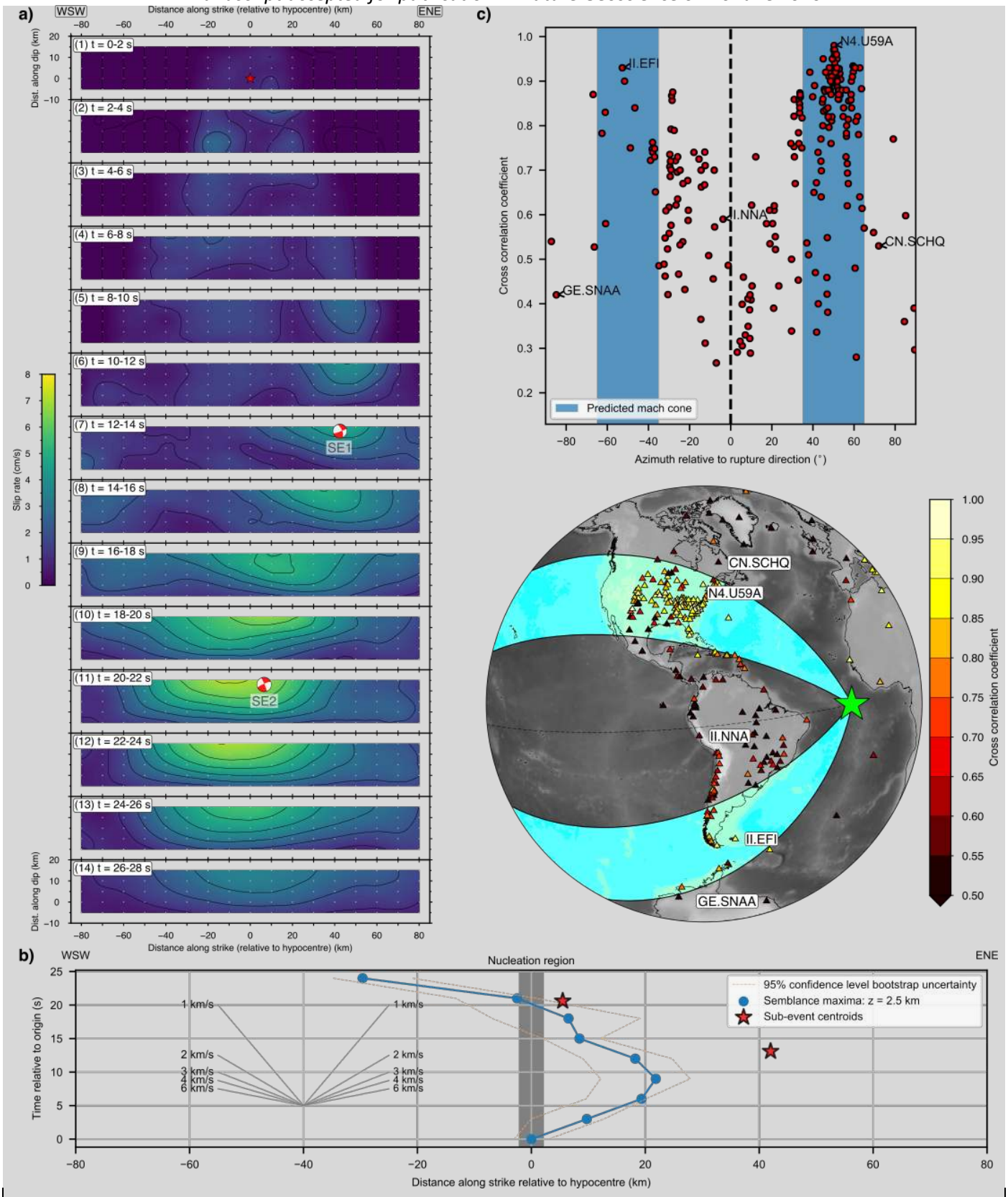

Figure 3: Teleseismic analyses. a) Slip-rate evolution over time along the fault, given in two-second interval steps (labelled in the top-left corner), from teleseismic P-wave inversion. b) Along-strike position (relative to the hypocentre) and timing of high-frequency radiators (blue circles) and estimated uncertainty, sampled at 3 s time-steps. c) Results from Rayleigh wave Mach cone analysis. Cross-correlation coefficient values plotted versus azimuth relative to rupture direction (top) in map view (bottom). The coloured region in the map indicates the estimated Mach cone area. Waveforms from labelled stations are shown in **Extended Data Figure 1**.

Alternatively, if the rupture changed direction following SE1, then this part of the earthquake must have travelled at super-shear v_r (5–6 km/s). To validate this model, we used time-domain teleseismic back-projection (BP) imaging[27] with phase-weighted stacking of virtual seismic arrays (see **Methods**). We imaged the BP on two planar grids: one at 2.5 km depth and the other at 10 km depth below the seafloor. For the nucleation phase, we find a higher coherence of back-projected waves using the 10 km depth grid, consistent with rupture initiation in mantle. For the total rupture, the shallower grid has higher waveform coherence, indicating slip at crustal levels. The overall BP results (**Supplementary Video S1**) confirm an apparent reversal in rupture direction with an initial, eastwards propagation followed by a westerly-travelling phase travelling at 4–6 km/s (**Figure 3b).** Whilst the high-frequency radiators occur over a laterally more compact region than the sub-events and teleseismic slip-rate model, the overall pattern is consistent.

We verify this result by searching for far-field Rayleigh Mach waves[28,29] by comparing waveforms filtered at 10–20 s period from the Romanche mainshock with a co-located M_w 5.6 earthquake on 2018-02-15 that had an identical faulting mechanism[30] (**Figure 1**; see **Methods**). At azimuths of 35–65° relative to rupture direction, many stations have very high waveform similarity between the mainshock and aftershock with cross-correlations exceeding 0.9 (**Figure 1, Extended Data Figure 1**). Accounting for phase velocity variations over large epicentral distances of up to 90° (**Figure S14**), these azimuths demarcate a Mach cone with lower rupture directivity effects[28,29], similar to that predicted for a v_r of 5.7 km/s (see **Methods**; **Extended Data Figure 2**). Outside of the predicted Mach cone azimuths, waveform similarity is lower with cross-correlation coefficients generally less than 0.80 (**Figure 3c**; **Extended Data Figure 1**). A relatively low density of aftershocks in the super-shear segment (**Figure 2a**) is similar to past observations of super-shear earthquakes[31]. These indications of super-shear rupture appear to rule out the possibility of bilateral rupture from the hypocentre.

A remaining issue is whether after nucleation ($\Delta t = 0$–9 s) the rupture front was continuous, or SE1 was dynamically triggered due to S-waves from the initiation phase. The latter model, in which rupture nucleation may be regarded as a foreshock, is supported by the along-fault nodal maximum in S-wave amplitude and apparent $v_r \approx 3.5$–4 km/s, similar to the shear-wave velocity (v_S) of mid-to-lower crust. Yet OBS waveforms show continuous seismic energy radiation over time following rupture nucleation (**Figure S15**), suggesting a spreading, continuous rupture as indicated by BP imaging, although we cannot completely rule out dynamic triggering at smaller scales[32].

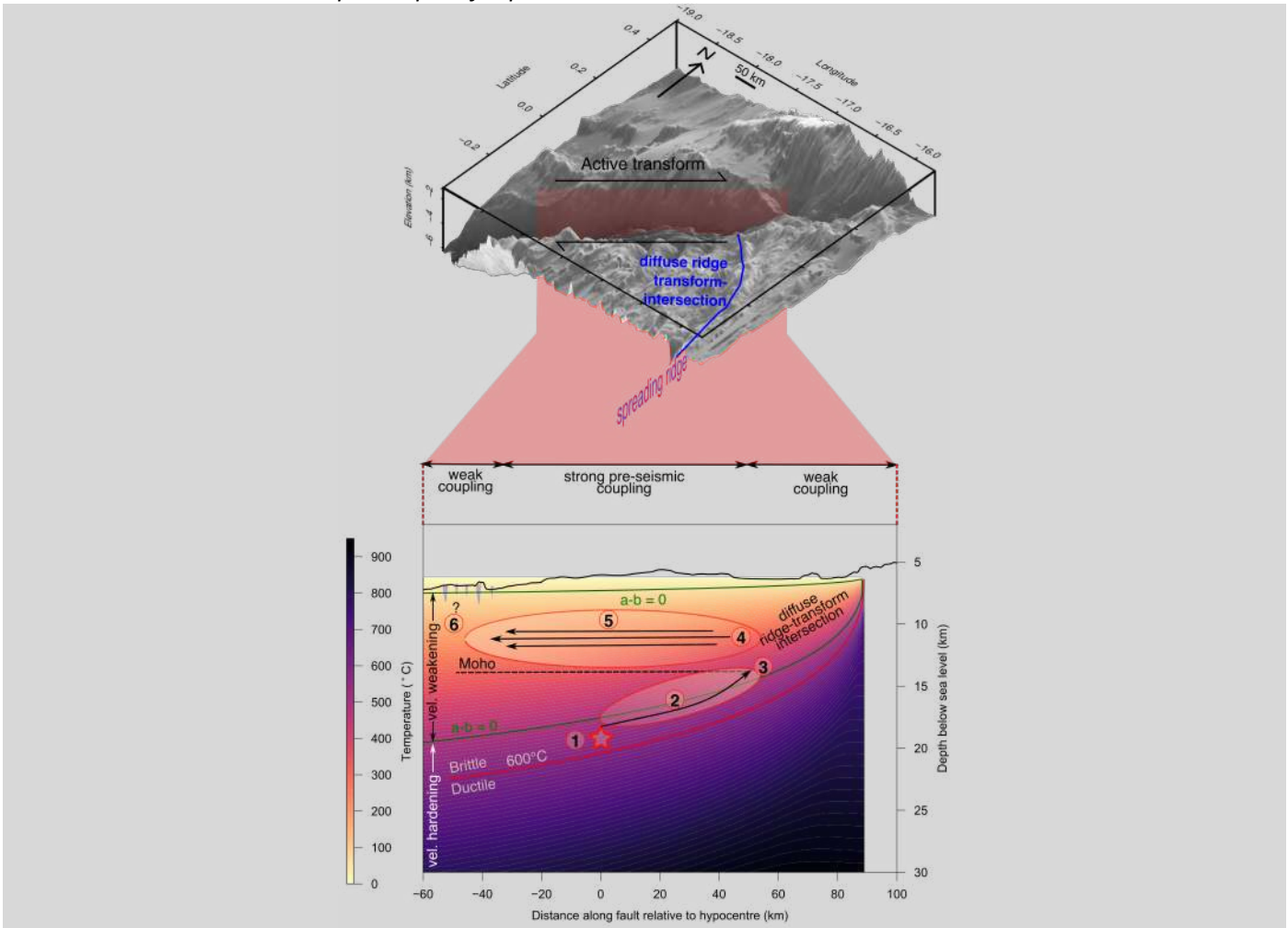

Figure 4: Interpretation of rupture dynamics for the 2016 Romanche earthquake. Top: perspective view of bathymetry along the Romanche FZ. Bottom: interpretive cut-through along the ruptured fault plane. Colours show a thermal profile based on half-space cooling. The green line denotes the predicted transition between velocity-strengthening and velocity-weakening frictional regimes from Gabbro data[35]. Labelled numbers show the key stages of rupture evolution as follows. (1) Rupture initiation (star) in oceanic mantle. (2) Initiation phase has sufficient fracture energy to propagate upwards to the locked section of fault. (3) Weak sub-shear rupture front travels east in the lower crust / upper mantle. (4) Rupture reaches the locked, thinner crustal segment close to the weaker ridge-transform intersection (SE1). (5) Sufficient fracture energy for westwards super-shear rupture in crust along strongly coupled fault segment (SE2). (6) Rupture possibly terminated by serpentinised and hydrothermally-altered fault segment.

Segmentation in fault stress controls rupture propagation

The unique spatio-temporal evolution of the 2016 Romanche earthquake adds new understanding to the geological controls on seismic slip along mature strike-slip faults, providing direct evidence of super-shear rupture along OTFs. Theoretical studies have suggested that earthquakes on inhomogeneous faults rupture in a preferred direction for sub- and super-shear propagation[33]. The segment that failed in 2016 is likely bi-material since it offsets crust with an age difference of ~27 Ma (**Figure 1**). If we assume higher seismic velocities on the older and cooler north side, the preferred super-shear direction[33] is east, opposite to our observations. This finding indicates that propagation direction might not be simply controlled by broad plate age and thermal variations. Instead, rupture direction may be more dependent on variable material properties within a wide (5–20 km) fault damage zone[12,13]. One possibility is that

greater fracturing and serpentinisation may exist on the older side, possibly related to uplift of the transverse ridge to the north[34], reducing seismic velocity, and resulting in preferred westward super-shear rupture.

The depth and lateral extent of rupture is likely determined in part by variations of serpentinisation in the seismogenic zone. The OBS data, teleseismic slip rate inversion and BP imaging imply deeper initiation at ~20 km depth. Therefore, the earthquake nucleated in the oceanic mantle, at the base of the seismogenic zone[5,35] at 500–600°C temperature (**Figure 4**). Nucleation was likely promoted by brittle failure in conditionally-stable serpentinised mantle peridotite[6]. Most seismic slip occurred in the crust beneath a topographically smoother segment of the Romanche axial valley (~6,200 m BSL; **Figure 2a**, **Figure 4**). At the rupture's western end, a deeper valley (>6,500 m) may indicate greater hypothermal alteration and serpentinsation[11,13], resulting in velocity-strengthening frictional behaviour[13,34]. The eastern edge of the rupture lies where the seafloor steepens to shallower depths of <5,500 m at the diffuse RTI (**Figure 2a**, **Figure 4**), which likely restricted slip due to a narrower seismogenic zone[35]. These fault segments bounding the earthquake likely creep aseismically, contributing to the overall low seismic coupling of OTFs[5].

Our preferred explanation for rupture reversal during the 2016 M_w 7.1 Romanche earthquake is as follows and illustrated in **Figure 4**. Nucleation occurred at ~20 km depth, above the brittle-ductile transition (**Figure 4**, Step 1-2). SE1 then ruptured along the ~500–600°C isotherm towards the surface near the RTI, with relatively weak slip in conditionally-stable serpentinised mantle peridotite[35] (**Figure 4**, Step 3-4). We speculate that the SE2 fault segment was pre-seismically more strongly coupled than for SE1, but its potential reactivation from a vertically propagating rupture front with little strain energy release was buffered by altered mantle peridotite. SE1 then provided sufficient strain energy release to overcome the larger fracture energy of the locked SE2 segment, resulting in super-shear rupture and termination in an adjacent weak zone (**Figure 4**, Step 5-6). Either both fault patches were sufficiently pre-seismically stressed to promote seismogenic failure[36], or the deeper SE1 rupture instantaneously increased the static stress, immediately causing the shallow SE2 portion of the fault to fail.

Observations of back-propagating ruptures along single isolated faults are sparse[37,38], although rapid tremor reversals can occur in subduction settings[39]. Our observations are supported by dynamic simulations in which the presence of a wide, low-velocity damage zones, such as those along OTFs[12,13], promotes back-propagating rupture fronts[40]. Alternatively, multiple fault strands in such a wide damage zone may also help to facilitate a reversing earthquake. Another possible explanation for the Romanche earthquake is that a cascading rupture reversal can occur when a weak nucleation phase starts in the mantle, and away from a barrier on one side of the fault. In this case, rupture directionality depends on interactions between the nucleation point, strain release history, and fracture energy variations along the fault. Whilst it has been suggested that seismogenic stresses on OTFs are highly deterministic[9-11], our result implies that OTF earthquakes, even with long-lived asperity-barrier segmentation, may resemble those of continental strike-slip earthquakes, without requiring orthogonal fault systems.

Our study implies that growing propagation in one direction may not be deterministic of a later emerging larger rupture travelling in the opposite direction. Thus, if back-propagating rupture fronts occur during earthquakes along

continental faults[37,38], predictions of ground shaking intensity and duration, such as those made by earthquake early warning systems, could be impacted.

References

1. Zhang, H., Koper, K. D., Pankow, K. & Ge, Z. Imaging the 2016 Mw 7.8 Kaikoura, New Zealand, earthquake with teleseismic P waves: A cascading rupture across multiple faults. *Geophys. Res. Lett.* **44**, 4790–4798 (2017).

2. Meng, L. *et al.* Earthquake in a Maze: Compressional Rupture Branching During the 2012 Mw 8.6 Sumatra Earthquake. *Science* **337**, 724 726 (2012).

3. Hicks, S. P. & Rietbrock, A. Seismic slip on an upper-plate normal fault during a large subduction megathrust rupture. *Nat. Geosci.* **8**, 955 960 (2015).

4. Ross, Z. E. *et al.* Hierarchical interlocked orthogonal faulting in the 2019 Ridgecrest earthquake sequence. *Science* **366**, 346–351 (2019).

5. Boettcher, M. & Jordan, T. Earthquake scaling relations for mid-ocean ridge transform faults. *J. Geophys. Res.* **109**, 74 (2004).

6. Kuna, V. M., Nábělek, J. L. & Braunmiller, J. Mode of slip and crust–mantle interaction at oceanic transform faults. *Nat. Geosci.* **12**, 138 (2019).

7. Sykes, L. R. & Ekström, G. Earthquakes along Eltanin transform system, SE Pacific Ocean: fault segments characterized by strong and poor seismic coupling and implications for long-term earthquake prediction. *Geophys. J. Int.* **188**, 421 434 (2012).

8. Froment, B. *et al.* Imaging along-strike variations in mechanical properties of the Gofar transform fault, East Pacific Rise. *J. Geophys. Res.* **119**, 7175 7194 (2014).

9. McGuire, J. J., Boettcher, M. S. & Jordan, T. H. Foreshock sequences and short-term earthquake predictability on East Pacific Rise transform faults. *Nature* **434**, 457 461 (2005).

10. McGuire, J. Seismic Cycles and Earthquake Predictability on East Pacific Rise Transform Faults. *B. Seismol. Soc. Am.* **98**, 1067–1084 (2008).

11. Roland, E. & McGuire, J. J. Earthquake swarms on transform faults. *Geophys. J. Int.* **178**, 1677–1690 (2009).

12. Avendonk, V. H., Harding, A., Orcutt, J. & McClain, J. Contrast in crustal structure across the Clipperton transform fault from travel time tomography. *J. Geophys. Res.* **106**, 10961 10981 (2001).

13. Roland, E., Lizarralde, D., McGuire, J. J. & Collins, J. A. Seismic velocity constraints on the material properties that control earthquake behavior at the Quebrada-Discovery-Gofar transform faults, East Pacific Rise. *J Geophys. Res.* **117**, B11102 (2012).

14. Schwehr, M., Boettcher, M. S., McGuire, J. J. & Collins, J. A. The relationship between seismicity and fault structure on the Discovery transform fault, East Pacific Rise. *Geochem. Geophys. Geosystems* **15**, 3698 3712 (2014).

15. Duputel, Z., Tsai, V. C., Rivera, L. & Kanamori, H. Using centroid time-delays to characterize source durations and identify earthquakes with unique characteristics. *Earth. Planet. Sci. Lett.* **374**, 92–100 (2013).

16. Abercrombie, R. E. & Ekström, G. Earthquake slip on oceanic transform faults. *Nature* **410**, 74 77 (2001).

17. Antolik, M., Abercrombie, R. E., Pan, J. & Ekström, G. Rupture characteristics of the 2003 Mw 7.6 mid-Indian Ocean earthquake: Implications for seismic properties of young oceanic lithosphere. *J. Geophys. Res.* **111**, B04302 (2006).

18. Aderhold, K. & Abercrombie, R. E. The 2015 Mw 7.1 earthquake on the Charlie-Gibbs transform fault: Repeating earthquakes and multimodal slip on a slow oceanic transform. *Geophys. Res. Lett.* **43**, 6119-6128 (2016).

19. Wang, D., Mori, J. & Koketsu, K. Fast rupture propagation for large strike-slip earthquakes. *Earth. Planet. Sci. Lett.* **440**, 115 126 (2016).

20. Yue, H. *et al.* Supershear rupture of the 5 January 2013 Craig, Alaska (Mw 7.5) earthquake. *J. Geophys. Res.* **118**, 5903-5919 (2013).

21. Huang, Y., Ampuero, J.-P. & Helmberger, D. V. The potential for supershear earthquakes in damaged fault zones – theory and observations. *Earth. Planet. Sci. Lett.* **433**, 109–115 (2016).

22. Bouchon, M., Karabulut, H., Bouin, M.-P., Schmittbuhl, J., Vallée, M., Archuleta, R., Das, S., Renard, F. & Marsan, D., Faulting characteristics of supershear earthquakes, Tectonophysics, 493(3–4), 244–253 (2010).

23. Sokos, E. N. & Zahradnik, J. ISOLA a Fortran code and a Matlab GUI to perform multiple-point source inversion of seismic data. *Comput. Geosci.* **34**, 967 977 (2007).

24. Vallée, M., Charléty, J., Ferreira, A., Delouis, B. & Vergoz, J. SCARDEC: a new technique for the rapid determination of seismic moment magnitude, focal mechanism and source time functions for large earthquakes using body-wave deconvolution. *Geophys J. Int.* **184**, 338 358 (2011).

25. Shimizu, K., Yagi, Y., Okuwaki, R. & Fukahata, Y. Development of an inversion method to extract information on fault geometry from teleseismic data. *Geophys. J. Int.* **220**, 1055–1065 (2020).

26. Prieto, G. A., Froment, B., Yu, C., Poli, P. & Abercrombie, R. Earthquake rupture below the brittle-ductile transition in continental lithospheric mantle. *Sci. Adv.* **3**, e1602642 (2017).

27. Krüger, F. & Ohrnberger, M. Tracking the rupture of the Mw = 9.3 Sumatra earthquake over 1,150 km at teleseismic distance. *Nature* **435**, 937–939 (2005).

28. Vallée, M. & Dunham, E. Observation of far-field Mach waves generated by the 2001 Kokoxili supershear earthquake. *Geophys. Res. Lett.* **39**, L05311 (2012).

29. Bao, H. *et al.* Early and persistent supershear rupture of the 2018 magnitude 7.5 Palu earthquake. *Nat. Geosci.* **12**, 200–205 (2019).

30. Ekström, G., Nettles, M. & Dziewoński, A. The global CMT project 2004–2010: Centroid-moment tensors for 13,017 earthquakes. *Phys. Earth. Planet. Int.* **200**–**201**, 1–9 (2012).

31. Bouchon, M., and H. Karabulut, The aftershock signature of supershear earthquakes, Science, 320 (5881), 1323–1325 (2008).

32. Wang, D., Mori, J. & Uchide, T. Supershear rupture on multiple faults for the Mw 8.6 Off Northern Sumatra, Indonesia earthquake of April 11, 2012. *Geophys. Res. Lett.* **39**, L21307 (2012).

33. Xia, K., Rosakis, A. J., Kanamori, H. & Rice, J. R. Laboratory Earthquakes Along Inhomogeneous Faults: Directionality and Supershear. *Science* **308**, 681–684 (2005).

34. Bonatti, E. *et al.* Transform migration and vertical tectonics at the Romanche fracture zone, equatorial Atlantic. *J. Geophys. Res.* **99**, 21779-21802 (1994).

35. Liu, Y., McGuire, J. J. & Behn, M. D. Frictional behavior of oceanic transform faults and its influence on earthquake characteristics. *J. Geophys. Res.* **117**, B04315 (2012).

36. Michel, S., Avouac, J.-P., Lapusta, N. & Jiang, J. Pulse-like partial ruptures and high-frequency radiation at creeping-locked transition during megathrust earthquakes. *Geophys. Res. Lett.* **44**, 8345–8351 (2017).

37. Meng, L., Ampuero, J. P., Page, M. T., & Hudnut, K. W. Seismological evidence and dynamic model of reverse rupture propagation during the 2010 M7.2 El Mayor Cucapah earthquake, Abstract presented at 2012 Fall Meeting, AGU, San Francisco, CA (2012).

38. Beroza, G. C., & Spudich, P. Linearized inversion for fault rupture behavior: Application to the 1984 Morgan Hill, California, earthquake. J. Geophys. Res, 93(B6), 6275-6296 (1988).

39. Yamashita, Y., Yakiwara, H., Asano, Y., Shimizu, H., Uchida, K., Hirano, S., Umakoshi, K., Miyamachi, M., Nakamoto, M., Fukui, M., Kamizono, M., Kanehara, H., Yamada., T., Shinohara, M. & Obara, K. Migrating tremor off southern Kyushu as evidence for slow slip of a shallow subduction interface. Science, 348(6235), 676-679 (2015).

40. Idini, B., & Ampuero, J. P. Fault-zone damage promotes pulse-like rupture and rapid-tremor-reversals. Preprint at https://eartharxiv.org/v8xr2/ (2019).

Corresponding author

Correspondence should be addressed to S.P.H. (email: s.hicks@imperial.ac.uk).

Acknowledgments

We thank the captain and crew of the R/V Marcus Langseth and the RRS Discovery and also the scientific technicians. Funding: S.P.H. was funded by the Natural Environment Research Council (NERC) grant NE/K010654/1; C.A.R., N.H., P.B. acknowledge funding from NERC (NE/M003507/1 and NE/K010654/1) and the European Research Council (GA 638665); J.M.K. and D.S. were funded by NERC (NE/M004643/1). A.S and H.S. thank the German Research Foundation DFG for funding through an Emmy-Noether Young-Researcher-Grant (#276464525). J.Z. was supported by the Czech Science Foundation Grant GACR-18-06716J. We thank the captain and crew of the R/V Marcus G. Langseth and the RRS Discovery and also the scientific technicians. We thank Martin Mai and one anonymous reviewer for taking the time to provide very useful feedback. Tim Craig also provided useful comments.

Author contributions

S.P.H. managed the study, carried out the mainshock and aftershock source analysis, and wrote the manuscript. R.O. computed the teleseismic slip-rate inversion, assisted with the Mach cone analysis and contributed to the manuscript. A.S. and H.S. computed the teleseismic back-projection images and contributed to the manuscript. C.R., N.H. and JMK conceived the experiment, acquired, funding, managed the project, and contributed to the manuscript. R.E.A carried out a preliminary teleseismic slip inversion and contributed to the manuscript. P.G. and D.S. worked on early estimates of source depth, assisted with aftershock detection and relocation, and commented on the manuscript. J.Z. assisted with the RMT inversions and contributed to the manuscript. Y.Y. and K.S. assisted with the teleseismic slip-rate inversion and commented on the manuscript.

Methods

Data: Local OBS network

We deployed 39 broadband OBS stations in March 2016 for twelve months as part of the PI-LAB (Passive Imaging of the Lithosphere-Asthenosphere Boundary) and the EURO-LAB (Experiment to Unearth the Rheological Oceanic Lithosphere-Asthenosphere Boundary) experiments (see **Note S1** & **Data Availability**). The network centred on the Chain Fracture Zone, next to Romanche, provides good coverage of the eastern end of the Romanche OTF (**Figure S1**). Due to instrument issues at some stations, not all sensor components for each station were used in this study.

Mainshock hypocentre and aftershock relocation

For hypocentre relocation, we used a 1-D layered P-wave velocity model for the central Atlantic from CRUST1.0[41], and a constant v_p/v_s ratio of 1.71 (See **Note S2**). We used the NonLinLoc package[42] for hypocentre relocations in which we employed a travel-time dependent error, which effectively gives an epicentral distance weighting. We used true depths below sea level of the OBS stations in the relocation. The epicentre lies NW of the PI-LAB OBS network, with the closest station 130 km away. Our epicentre is located <7 km away from those of other agencies that used teleseismic arrivals alone (**Table S1**), suggesting a robust estimation of the rupture nucleation position (**Figure S2**). Although the PI-LAB OBS network offers sub-optimal coverage of the rupture area, we are confident that the hypocentre locations are sufficiently accurate to probe the seismicity distribution along the fault (**Note S3**), although depths are poorly constrained. Next, we relocated 101 aftershocks and further refined these by performing a multiple-event relocation relative to the mainshock hypocentre (**Note S3**). We also scanned continuous waveforms at the closest three stations to find any foreshocks in the days leading up to the mainshock, but we found none within this period along the Romanche Fracture Zone. Eleven of these aftershocks are in the USGS-NEIC catalogue. See **Supplementary Data S1** for the full hypocentre and arrival time catalogue.

RMT inversion

For RMT inversion, we computed Green's functions (GF) in our layered velocity model using the discrete wavenumber method[43]. We used the ISOLA software package[23] (see **Code Availability**), which inverts for waveforms in the time domain to compute moment tensors. ISOLA searches across a prescribed grid of trial-point-sources to find the deviatoric centroid moment tensor in space and time that maximises the fit (given as variance reduction, *VR*) between synthetic and observed waveforms. We carefully chose waveforms unaffected by clipping and non-linear tilting due to the Romanche earthquake to stabilise the moment tensor solutions. We also tested the stability of inversion by jack-knifing waveform traces. We used stations located up to 700 km epicentral distance from the hypocentre of the Romanche mainshock. **Figure 1** shows the stations used for regional waveform inversion.

Based on initial CMT inversions, together with the mainshock hypocentre and the geometry of Romanche OTF from bathymetric data, we designed a grid of trial-point sources along a plane striking 75° and dipping 80° to the south-

east. The origin of the plane is given as our relocated hypocentre. We placed 16 sources along-strike (spacing of 6 km), and 6 sources in the down-dip direction (spacing of 4 km); (**Figure 2**).

We first inverted for a single-point source moment tensor solution using long-period waveforms (33–100 s period; **Figure S3).** Even with the suboptimal station coverage, the retrieved moment tensor solution is consistent with the faulting style along the Romanche FZ.

To investigate source complexity, we inverted waveforms at higher frequencies of 0.01 to 0.10 Hz. We used iterative deconvolution, which has been used extensively to probe rupture complexity at regional scales[3,44,45]. For each sub-event, we searched for length of the triangular source-time function that maximised VR. The centroid location of SE1 is better constrained than that of SE2 (**Figure S4**), which may reflect the long, fast rupture of SE2. We do not find any significant waveform pulse closer to the origin time, so we cannot robustly add a third sub-event, indicating comparatively less slip during the nucleation phase. This observation is in line with the 1994 Romanche earthquake[16]. In general, adding more than two subevents for this size of earthquake can be unstable does not improve the fit considerably[3].

To estimate an overall source-time function (STF) for the total rupture (**Figure 2c**), we inverted the waveforms in terms of 10 s long equidistantly-shifted isosceles triangle functions and apply a non-negative least square constraint (NNLS)[46]. We prescribe the CMT parameters for both sub-events as per the result above and fix the total moment.

See **Supplementary Data S2** for the optimum RMT parameters.

Teleseismic slip-rate inversion

We solved the spatio-temporal potency-density tensor distribution[25,47]. We represent slip along the fault with five-basis double-couple components so that we flexibly represent the slip vectors without forcing them to span an arbitrarily assumed model plane, which suppresses modelling errors due to the inappropriate assumption of the fault-plane geometry[25]. At every 1 s snapshot, the slip-rate function at each source node is represented by linear B-splines. Model parameters are objectively determined by minimising Akaike's Bayesian Information Criterion (ABIC)[48], which is expected to produce solutions similar to fully Bayesian inversions[49], since we do not adopt non-negative constraints for slip vectors (positivity constraint) in our ABIC-based inversion scheme.

Vertical components of teleseismic P waveforms were obtained (see **Data Availability**; **Supplementary Data S3**) and we selected 57 stations (**Figure S5**) that cover all azimuths to capture radiation patterns, and also chose stations with high signal-to-noise ratio so we could reliably pick P-wave first motions. The instrument responses were removed and the records were converted into velocity waveforms, and then we resampled the data to one sample per second. GFs were calculated with the near-source velocity structures adopted from CRUST1.0[41]. GFs were calculated with the near-source velocity structures adopted from CRUST1.0, and the attenuation time constant t* for the P wave was taken to be 1.0 s. We did not apply any filters to both the observed waveforms and the theoretical GFs following the inversion procedure[25]. We used the model plane striking at 79° and dipping at 77° based on the procedure for our regional CMT inversion and the relocated-aftershock distribution. The model plane was discretised into a grid spanning 10 km and

5 km along the strike and dip directions, respectively. Our relocated hypocentre of the mainshock was adopted for the initial rupture point. Guided by the position and timing of the sub-events from RMT inversion, the Mach cone analysis, and the BP imaging results, we set the total rupture duration as 30 s and the maximum rupture speed at 6.0 km/s. **Figure S3** shows the resulting teleseismic P-wave fits.

Synthetic tests and experiments using different fault-plane geometries produced a similar pattern of slip to the optimum solution (**Notes S5 and S6**). The overall source-time function also compares well with that derived from OBS waveforms (**Figure 2c**). We assessed the robustness of the optimum teleseismic slip model by testing different fault geometries (up to ±10° in strike and dip). In all fault geometry configurations, the overall pattern of the slip distribution is very similar to that of the optimum model (**Note S5**). We also forward modelled waveforms from our optimum smooth solution, added Gaussian noise at a level of 1% of the signal variance, and inverted these waveforms. This synthetic test (**Figure S12**) shows that the inversion is able to retrieve the main features of the rupture in space and time.

In raw teleseismic P-waves (**Figure S5**) small pulses following the initial P-wave are visible, with a broad pulse at $\Delta t =$ 10 s (SE1) particularly clear at WSW and ESE azimuths. This is followed by a larger pulse at $\Delta t = 20$ s (SE2). **Figure S5** shows the resulting teleseismic P-wave fits for our best-fitting model. The P-wave azimuthal variation of low-frequency teleseismic P-waves confirms that the larger slip patch (SE2) occurred west of the rupture nucleation (**Figure S6**).

Compared to an operational finite fault model for the 2016 Romanche earthquake from USGS-NEIC (https://earthquake.usgs.gov/earthquakes/eventpage/us20006uy6/finite-fault; last accessed June 2020), which requires low rupture velocity during the first 15 s of rupture, we found that a shallower, south-dipping fault substantially increased waveform fits at near-nodal stations.

Teleseismic back-projection imaging

We used the Palantiri software (see **Code Availability**) which clusters stations at teleseismic distances and generates virtual seismic arrays[27,50]. We calculate the travel-times between grid-points and stations using the ak135 velocity model and stack in 12-second-long moving windows (centred on each timestep) with respect to the expected P-wave onsets using the phase-weighting method[51]. We stack waveforms with respect to normalised semblance, which is a measure of the fraction of the radiated energy released as coherent waves. Semblance has sharper resolution than beampower for low-energy radiation and is less sensitive to amplitude effects due to site terms. The semblance from all virtual arrays is combined at each 3 s timestep for a total duration of 30 s (10 timesteps). To avoid an azimuthal bias, we subdivide all azimuthal directions around the epicentre into twelve sectors. The semblance from each azimuth sector is normalized to one, so that each azimuthal sector has the same influence on the combined semblance.

Bayesian bootstrapping of array weights is used to estimate the significance of the estimated location of the semblance. This means that the semblance is combined 100 times with randomised Bayesian weights for each array and with slightly perturbed velocity models such that arrival times may vary by +/- 4s.

In total, 345 stations (see **Data Availability**; **Supplementary Data S4**) are clustered using the *k*-means algorithm into 27 virtual arrays with a maximum aperture of 5° (**Figure S13**). We use velocity waveform recordings down-sampled to 10 Hz, and to investigate the high-frequency emissions we bandpass filter between 0.2 Hz and 1.5 Hz. Stations for which waveforms have a correlation coefficient <0.6 relative to the centremost station of each virtual array are not used.

Rayleigh wave Mach cone analysis

Past theoretical and observational studies[28,29] have shown that the effect of rupture directivity on surface waves can be used to determine rupture velocity. For earthquakes rupturing at velocities slower than seismic wave speed, waves from the start and end of rupture arrive at a far-field receiver at variable times. However, for super-shear earthquakes, at stations located on the Mach cone, the waves from different parts of the rupture arrive at the same time. These simultaneous arrivals result in surface waves that are highly correlated with those of a smaller, co-located earthquake with identical faulting mechanism that can be viewed as a point-source at the periods considered.

The range of azimuths where high waveform correlation can be observed depends on several factors: rupture direction, speed and duration, Rayleigh wave velxocity, and frequency band. Given the source duration of SE2 of ~25 s (**Figure 3c**), we can only see a substantial azimuthal variation in directivity factor at frequencies above the corner frequency. Therefore, we bandpass filter teleseismic waveforms up to 90° epicentral distance (see **Data Availability**; Source Data Fig 3c) between 10 s and 20 s period. We estimate Rayleigh wave phase velocities from the GDM52 model[52]. GDM52 gives velocities at a minimum period of 25 s – a longer period than that of our filtered waveforms; given the large variation in velocities along the long surface wave paths (typically 40–90° distance; **Figure S14**), we choose a mean surface wave velocity of 3.4 km/s for the shorter periods considered in this study. Taking a short-period cut-off filter corner at 10 s, and assuming a mean along-path Rayleigh wave phase velocity of 3.4 km/s, we predict a high waveform similarity - i.e. a small directivity factor - at azimuths of 35–65° with respect to the rupture direction (**Extended Data Figure 2**).

Our Rayleigh wave Mach Cone analysis for the 1994 M_w 7.1 Romanche earthquake[16] also hints at super-shear rupture (**Figure S16**).

Data availability

The facilities of IRIS Data Services, and specifically the IRIS Data Management Center (IRIS-DMC), were used for access to waveforms, related metadata, and/or derived products used in this study. IRIS Data Services are funded through the Seismological Facilities for the Advancement of Geoscience (SAGE) Award of the National Science Foundation under Cooperative Support Agreement EAR-1851048. Additional seismic data were obtained from the GEOFON data centre of the GFZ German Research Centre for Geosciences (GFZ-GEOFON), ORFEUS/EIDA, the INGV Seismological Data Centre, and the RESIF Data Center.

RESIF is a national Research Infrastructure, recognised as such by the French Ministry of Higher Education and Research. RESIF is managed by the RESIF Consortium, composed of 18 Research Institutions and Universities in France. RESIF additionally supported by a public grant overseen by the French National Research Agency (ANR) as part of the "Investissements d'Avenir" program (reference: ANR-11-EQPX-0040) and the French Ministry of Ecology, Sustainable Development and Energy.

Continuous raw seismic waveform data from the PI-LAB ocean bottom seismometer network[53] can be downloaded from IRIS-DMC (network code XS).

Continuous raw seismic waveform data from various global seismic networks used for the slip-rate inversion[54-61], back-projection[54-81], and Mach cone[54,56-60,67-70,79,82-103] analyses are available to download from the data centres named above.

Code availability

The ISOLA software used for RMT inversion is available from http://geo.mff.cuni.cz/~jz/for_ISOLAnews/ (last accessed June 2020). The Palantiri software used for teleseismic back-projection analysis is available from https://braunfuss.github.io/Palantiri/ (last accessed June 2020). We used the ObsPy package for seismic analysis[104]. Figures were made using GMT[105] and matplotlib[106].

Extended Data Figures

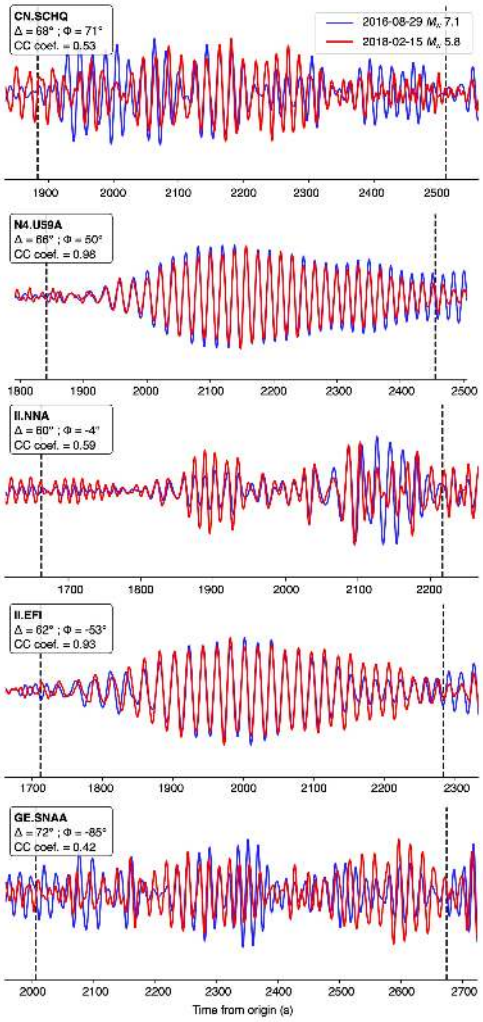

Extended Data Figure 1: Rayleigh wave vertical displacement seismograms. Waveforms are plotted for the M_w 7.1 Romanche mainshock and M_w 5.8 co-located aftershock, for stations shown in **Figure 3b**. The top-left box indicates the network code, station name, epicentral distance, azimuth relative to rupture direction, and cross-correlation value. Stations N4.N59A and II.EFI are located in the predicted Mach cone.

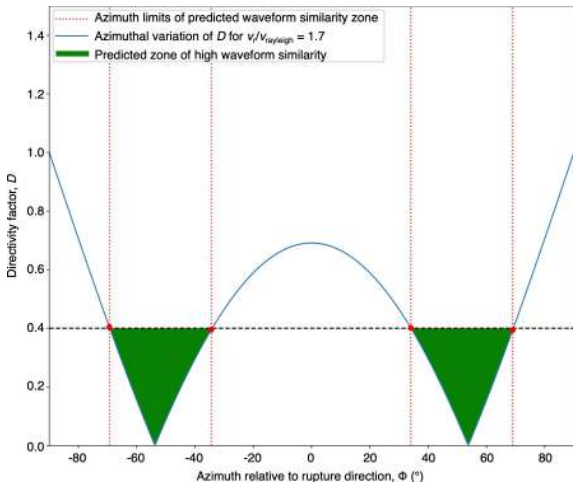

Extended Data Figure 2: Predicted Mach cone. Azimuthal dependence of directivity factor (blue line) for a rupture velocity of 5.7 km/s, period of 10 s, rupture duration of 25 s and Rayleigh wave velocity of 3.4 km/s. The black-dashed line, red dashed lines, and green shaded areas demarcate azimuths where high waveform similarity between the Romanche mainshock and co-located aftershock can be found. These azimuth values correspond well to the locations where high waveform similarity is observed in the data (**Figure 3b**).

Additional References

41. Laske, G., Masters, G., Ma, Z. & Pasyanos, M. Update on CRUST1. 0—A 1-degree global model of Earth's crust. *Geophys. Res. Abstr* **15**, 2658 (2013).

42. Lomax, A., Virieux, J., Volant, P. & Berge-Thierry, C. Probabilistic Earthquake Location in 3D and Layered Models. *Advances in Seismic Event Location* **18**, 101-134 (2000).

43. Bouchon, M. A simple method to calculate Green's functions for elastic layered media. Bull. Seismol. Soc. Am. 71, 959–971 (1981).

44. Bie, L., Hicks, S., Garth, T., Gonzalez, P. & Rietbrock, A. 'Two go together': Near-simultaneous moment release of two asperities during the 2016 Mw 6.6 Muji, China earthquake. *Earth Planet. Sci. Lett.* **491**, 34-42 (2018).

45. Zahradník, J. *et al.* A recent deep earthquake doublet in light of long-term evolution of Nazca subduction. *Sci. Rep.* **7**, 45153 (2017).

46. Zahradnik, J. & Sokos, E. N. The Mw 7.1 Van, Eastern Turkey, earthquake 2011: two-point source modelling by iterative deconvolution and non-negative least squares. *Geophys. J. Int.* **196**, 522 538 (2014).

47. Yagi, Y. & Fukahata, Y. Introduction of uncertainty of Green's function into waveform inversion for seismic source processes. *Geophys. J. Int.* **186**, 711-720 (2011).

48. Yabuki, T. & Matsu'ura, M. Geodetic data inversion using a Bayesian information criterion for spatial distribution of fault slip. *Geophys. J. Int.* **109**, 363–375 (1992).

49. Fukuda, J. & Johnson, K. A Fully Bayesian Inversion for Spatial Distribution of Fault Slip with Objective Smoothing. *B. Seismol. Soc. Am.* **98**, 1128-1146 (2008).

50. Roessler, D., Krueger, F., Ohrnberger, M. & Ehlert, L. Rapid characterisation of large earthquakes by multiple seismic broadband arrays. *Nat. Hazards Earth Syst. Sci.* **10**, 923–932 (2010).

51. Schimmel, M. & Paulssen, H. Noise reduction and detection of weak, coherent signals through phase-weighted stacks. *Geophys J. Int.* **130**, 497–505 (1997).

52. Ekström, G. A global model of Love and Rayleigh surface wave dispersion and anisotropy, 25–250 s. *Geophys J. Int.* **187**, 1668–1686 (2011).

53. Rychert, C., J Michael Kendall, & Harmon, N. Passive Imaging of the Lithosphere-Asthenosphere Boundary [Data set]. International Federation of Digital Seismograph Networks. https://doi.org/10.7914/SN/XS_2016. (2016).

54. Geological Survey Of Canada. Canadian National Seismograph Network. International Federation of Digital Seismograph Networks. https://doi.org/10.7914/SN/CN. (1989).

55. Institute Of Geophysics, A. O. S. O. T. C. R. Czech Regional Seismic Network. International Federation of Digital Seismograph Networks. https://doi.org/10.7914/SN/CZ. (1973).

56. Institut De Physique Du Globe De Paris (IPGP), & Ecole Et Observatoire Des Sciences De La Terre De Strasbourg (EOST). GEOSCOPE, French Global Network of broad band seismic stations. Institut de Physique du Globe de Paris (IPGP). https://doi.org/10.18715/GEOSCOPE.G. (1982).

57. GEOFON Data Centre. GEOFON Seismic Network. Deutsches GeoForschungsZentrum GFZ. https://doi.org/10.14470/TR560404. (1993).

58. Albuquerque Seismological Laboratory (ASL)/USGS. Global Telemetered Seismograph Network (USAF/USGS). International Federation of Digital Seismograph Networks. https://doi.org/10.7914/SN/GT. (1993).

59. Scripps Institution Of Oceanography. IRIS/IDA Seismic Network. International Federation of Digital Seismograph Networks. https://doi.org/10.7914/SN/II. (1986).

60. Albuquerque Seismological Laboratory (ASL)/USGS. Global Seismograph Network (GSN - IRIS/USGS). International Federation of Digital Seismograph Networks. https://doi.org/10.7914/SN/IU. (1988).

61. MedNet Project Partner Institutions. Mediterranean Very Broadband Seismographic Network (MedNet). Istituto Nazionale di Geofisica e Vulcanologia (INGV). https://doi.org/10.13127/SD/fBBBtDtd6q. (1990).

62. Swiss Seismological Service (SED) At ETH Zurich. National Seismic Networks of Switzerland. ETH Zürich. https://doi.org/10.12686/sed/networks/ch. (1983).

63. Instituto Geofisico Escuela Politecnica Nacional (IG-EPN Ecuador). Ecuador Seismic Network [Data Set]. International Federation of Digital Seismograph Networks. http://www.fdsn.org/networks/detail/EC/. (2002).

64. Federal Institute for Geosciences and Natural Resources (BGR). German Regional Seismic Network (GRSN). Federal Institute for Geosciences and Natural Resources (BGR). https://doi.org/10.25928/mbx6-hr74. (1976).

65. Instituto Nacional De Sismologia, Vulcanologia, Meteorologia E Hidrologia (INSIVUMEH). Red Sismologica Nacional [Data set]. International Federation of Digital Seismograph Networks. https://doi.org/10.7914/SN/GI. (2013).

66. Kövesligethy Radó Seismological Observatory (Geodetic And Geophysical Institute, Research Centre For Astronomy And Earth Sciences, Hungarian Academy Of Sciences (MTA CSFK GGI KRSZO)). Hungarian National Seismological Network. Deutsches GeoForschungsZentrum GFZ. https://doi.org/10.14470/UH028726. (1992).

67. Lamont Doherty Earth Observatory (LDEO), Columbia University. Lamont-Doherty Cooperative Seismographic Network [Data set]. International Federation of Digital Seismograph Networks. https://doi.org/10.7914/SN/LD. (1970).

68. Universidad Nacional Autónoma de México (UNAM). Servicio Sismologico Nacional. [Data set]. https://doi.org/10.21766/SSNMX/SN/MX. (2017).

69. UC San Diego. Central and Eastern US Network. International Federation of Digital Seismograph Networks. https://doi.org/10.7914/SN/N4. (2013).

70. Saint Louis University. Cooperative New Madrid Seismic Network [Data set]. International Federation of Digital Seismograph Networks. http://www.fdsn.org/networks/detail/NM/. (1980).

71. Instituto Nicaraguense De Estudios Territoriales (INETER). *Nicaraguan Seismic Network*. Instituto Nicaraguense de Estudios Territoriales (INETER). https://doi.org/10.7914/SN/NU. (1975).

72. ZAMG-Zentralanstalt Für Meterologie Und Geodynamik. Austrian Seismic Network. International Federation of Digital Seismograph Networks. https://doi.org/10.7914/SN/OE. (1987).

73. Protti, M. Observatorio Vulcanológico y Sismológico de Costa Rica [Data set]. International Federation of Digital Seismograph Networks. https://doi.org/10.7914/SN/OV. (1984).

74. OGS (Istituto Nazionale Di Oceanografia E Di Geofisica Sperimentale). North-East Italy Seismic Network. International Federation of Digital Seismograph Networks. https://doi.org/10.7914/SN/OX. (2016).

75. Red Sismica Volcan Baru. ChiriNet [Data set]. International Federation of Digital Seismograph Networks. https://doi.org/10.7914/SN/PA. (2000).

76. Penn State University. Pennsylvania State Seismic Network. International Federation of Digital Seismograph Networks. https://doi.org/10.7914/SN/PE. (2004).

77. Geological Survey of Canada. Portable Observatories for Lithospheric Analysis and Research Investigating Seismicity (POLARIS) [Data set]. http://www.polarisnet.ca/network/polaris-network-locations.html. (2000).

78. Servicio Nacional de Estudios Territoriales (SNET), El Salvador. International Federation of Digital Seismograph Networks. http://www.snet.gob.sv/ver/sismologia. (2004).

79. IRIS Transportable Array. USArray Transportable Array. International Federation of Digital Seismograph Networks. https://doi.org/10.7914/SN/TA. (2003).

80. Red Sismológica Nacional de Costa Rica (RSN: UCR-ICE). Universidad De Costa Rica. https://doi.org/10.15517/TC. (2016).

81. University of Western Ontario (UWO Canada). The Southern Ontario Seismic Network [Data Set]. International Federation of Digital Seismograph Networks. http://www.fdsn.org/networks/detail/WU/. (1991).

82. Universidade de Sao Paulo, USP. Brazilian Lithospheric Seismic Project (BLSP) [Data set]. International Federation of Digital Seismograph Networks. http://www.fdsn.org/networks/detail/BL/. (1988).

83. University of Brasilia. University of Brasilia Seismic Network. International Federation of Digital Seismograph Networks. http://www.fdsn.org/networks/detail/BR/. (1995).

84. Universidad de Chile, Dept de Geofisica (DGF UChile Chile). Chilean National Seismic Network. International Federation of Digital Seismograph Networks. http://www.fdsn.org/networks/detail/C/. (1991).

85. California Institute Of Technology And United States Geological Survey Pasadena. Southern California Seismic Network. International Federation of Digital Seismograph Networks. https://doi.org/10.7914/SN/CI. (1926).

86. Servicio Geologico Colombiano. *Red Sismologica Nacional de Colombia* [Data set]. International Federation of Digital Seismograph Networks. https://doi.org/10.7914/SN/CM. (1993).

87. Albuquerque Seismological Laboratory (ASL)/USGS. *Caribbean USGS Network*. International Federation of Digital Seismograph Networks. https://doi.org/10.7914/SN/CU. (2006).

88. GFZ German Research Centre For Geosciences, & Institut Des Sciences De L'Univers-Centre National De La Recherche CNRS-INSU. IPOC Seismic Network. Integrated Plate boundary Observatory Chile - IPOC. https://doi.org/10.14470/PK615318. (2006).

89. GEUS Geological Survey of Denmark and Greenland. Danish Seismological Network. International Federation of Digital Seismograph Networks. http://www.fdsn.org/networks/detail/DK/. (1976).

90. National Seismological Centre Of Autonomous University Of Santo Domingo. CNS-UASD [Data set]. International Federation of Digital Seismograph Networks. https://doi.org/10.7914/SN/DR. (1998).

91. Instituto Geofisico Escuela Politecnica Nacional (IG-EPN Ecuador). Ecuador Seismic Network. International Federation of Digital Seismograph Networks. http://www.fdsn.org/networks/detail/EC/. (2002).

92. Geophysical Institute of Israel (GII Israel). Israel National Seismic Network. International Federation of Digital Seismograph Networks. http://www.fdsn.org/networks/detail/IS/. (1982).

93. INGV Seismological Data Centre. Rete Sismica Nazionale (RSN). Istituto Nazionale di Geofisica e Vulcanologia (INGV), Italy. https://doi.org/10.13127/SD/X0FXnH7QfY. (2006).

94. Albuquerque Seismological Laboratory (ASL)/USGS. Intermountain West Seismic Network. International Federation of Digital Seismograph Networks. https://doi.org/10.7914/SN/IW. (2003).

95. Institute Of Seismology, National Academy Of Sciences Of Kyrgyz Republic (KIS). Kyrgyz Digital Network. International Federation of Digital Seismograph Networks. https://doi.org/10.7914/SN/KR. (2007).

96. KNMI. *Caribbean Netherlands Seismic Network*. Royal Netherlands Meteorological Institute (KNMI). https://doi.org/10.21944/dffa7a3f-7e3a-3b33-a436-516a01b6af3f. (2006).

97. Utrecht University (UU Netherlands). *NARS* [Data set]. International Federation of Digital Seismograph Networks. https://doi.org/10.7914/SN/NR. (1983).

98. University Of Puerto Rico. Puerto Rico Seismic Network (PRSN) & Puerto Rico Strong Motion Program (PRSMP). International Federation of Digital Seismograph Networks. https://doi.org/10.7914/SN/PR. (1986).

99. New Mexico Tech. New Mexico Tech Seismic Network. International Federation of Digital Seismograph Networks. http://www.ees.nmt.edu/outside/Geop/NMTSO.html. (1999).

100. Albuquerque Seismological Laboratory (ASL)/USGS. United States National Seismic Network. International Federation of Digital Seismograph Networks. https://doi.org/10.7914/SN/US. (1990).

101. Fundación Venezolana De Investigaciones Sismológicas (FUNVISIS), Caracas. *Red Sismológica Satelital Nacional* [Data set]. International Federation of Digital Seismograph Networks. https://doi.org/10.7914/SN/VE. (2000).

102. Institut De Physique Du Globe De Paris- IPGP. GNSS, seismic broadband and strong motion permanent networks in West Indies. Institut de Physique du Globe de Paris - IPGP. https://doi.org/10.18715/antilles.WI. (2008).

103. INSN. Irish National Seismic Network, operated by the Dublin Institute for Advanced Studies and supported by the Geological Survey Ireland. International Federation of Digital Seismograph Networks. https://doi.org/10.7914/SN/EI. (1993).

104. Beyreuther, M., Barsch, R., Krischer, L., Megies, T., Behr, Y. & Wassermann, J. ObsPy: A Python Toolbox for Seismology. Seismol. Res. Lett., 81(3), 530-533 (2010).

105. Wessel, P., Luis, J. F., Uieda, L., Scharroo, R., Wobbe, F., Smith, W. H. F., & Tian, D. The Generic Mapping Tools version 6. Geochem., Geophys. Geosyst., 20, 5556–5564 (2019).

106. Hunter, J.D. Matplotlib: A 2D Graphics Environment". Computing in Science & Engineering, 9(3), 90-95 (2007).

Supplementary information to "Back-propagating super-shear rupture in the 2016 *Mw* 7.1 Romanche transform fault earthquake" by Stephen Hicks et al.

Supplementary Notes

S1 Details of the PI-LAB ocean-bottom seismometer (OBS) network

The network (**Figure S1**) comprised a mixture of OBS packages with three-component seismometers. Instruments came from Lamont-Doherty (120 s long-period response), Institut de Physique du Globe de Paris (120 s long-period response) and Scripps Institute of Oceanography (240 s long-period response). We computed the azimuths of horizontal seismometer components using automatic Rayleigh-wave polarisation analysis[1] and each station comprised a hydrophone or differential pressure gauge (DPG), also used for determining P-wave arrival times.

S2 Velocity model, arrival time picking and mainshock relocation

We chose a constant v_p/v_s of 1.71, which is consistent with reduced Wadati plot regression, and resulted in epicentres clustering along the surface trace of the Romanche OTF. A v_p/v_s ratio is also consistent with preliminary shear-wave velocity information from surface waves. Using a variable v_p/v_s ratio from CRUST1.0 resulted in more scattered hypocentre locations and less stable CMT solutions. The velocity model does not contain a sediment layer as <80 m thick sediment layers have been inferred for the deployment area[2].

We manually picked P-and S-wave arrivals at OBS stations, simultaneously solving for locations, using the SDX software[3]. We relocated the hypocentres using NonLinLoc[4]. The posterior probability density function offers a complete probabilistic solution to the earthquake location problem, including information on uncertainty and resolution. The closest OBS station is 120 km from the Romanche mainshock and the events lie outside the network (mean minimum azimuthal gap of 260°). However, with the likely homogeneous seismic velocity structure of oceanic plates, we believe the epicentral locations are robust. The low root-mean-square residual between theoretical and observed arrivals (RMS) for all events of <0.50 s supports this assumption as the furthest stations are >1,000 km away. The known strike of the fault, together with the fault-parallel azimuth of minimum axis epicentral uncertainty ellipse (**Figure S2**), due to the network geometry, gives a robust constraint on the rupture extent. To ensure that our location estimate was not biased by the possibility of S-wave arrival times mis-picked due to rupture complexity, we computed the hypocentre using P-waves arrivals alone, which produce a similar hypocentre location.

S3 Aftershock detection, catalogue and relocation

We formed a catalogue of aftershocks by first picking and analysing events in the ISC Bulletin in the region for three months after the mainshock. Additionally, we also took a preliminary set of automatic local event detections from the PILAB experiment based on the cluster-search algorithm of the SeisComp3 analysis package[5]. Due to the lack of station coverage, this automatic detection approach only captured a subset of the largest aftershocks; therefore, we also manually scanned continuous waveforms from the closest three stations (L02A, L33D, I34D) to detect aftershocks until 60 days after the mainshock. Overall, we relocated 101 events with well-constrained locations (RMS residual <0.8; maximum azimuthal gap < 270°). To provide a greater precision of aftershock epicentres, we then used the BayesLoc software[6] to perform a multiple-event relocation. We used all available local data from ocean-bottom seismometers and available teleseismic P arrivals from the ISC Bulletin. Then we performed a relative relocation by fixing the location of the mainshock and prescribing looser constraints on the aftershock origins based on the standard errors from NonLinLoc. Hypocentre depths of aftershocks remain very poorly constrained. Local magnitudes were computed using a generic M_L scale for California[7]. We find a good correlation between M_L, M_b, and M_w for the larger aftershocks. We recorded aftershocks with M_L = 3.0 to M_L = 4.8.

S4 Statistical significance of two sub-events in the RMT inversion

We assess the statistical significance of the second sub-event using an *F*-test[8]. We assume that samples are correlated over a period corresponding to the low-pass filter corner used in the inversion (10 s), and the dominant part of each waveform is ~150 s long, yielding 15 independent samples per component. For all 20 components (i.e. 300 data points) and subtracting the number of free parameters for a deviatoric moment tensor (7), we find that the increase in waveform fit is significant at the 95% confidence level.

S5 Teleseismic inversion sensitivity test with variable configuration of the model-plane geometry

Figure S7 shows a comparison of the resulting slip models using different inversion schemes. The effect of using different inversion schemes is shown (**Figure S8**, **Figure S9**, **Figure S10**, **Figure S11**) for different assumptions on the model fault geometry (see paragraph below for details). In each figure, Panel (a) shows the results of the conventional inversion scheme[9] with the double-couple components of the shear plane of each sub-fault patch constrained by the model plane. Figures in Panel (b) are the results from the preferred inversion scheme without forcing the shear plane to be the model plane, which we adopted in our study. As shown, there are systematic differences between the fixed and the non-fixed models. The key feature, however, of a long initial rupture stage followed by the main rupture propagating from east to west is resolved from both approaches.

We also tested the effect of unknown model-plane geometry by adding fluctuations of ±10° ±5° in strike and dip from the optimum model (strike: 79°; dip: 77°); (**Figure S8**, **Figure S9**, **Figure S10**, **Figure S11**). As shown, the fixed models are not stable against the assumption of the model-plane geometry, especially when dip angle is varied. In general,

especially for strike-slip earthquakes like the 2016 Romanche earthquake, the radiation pattern is sensitive to the nodal plane orientations, and the pre-fixed model-plane geometry may violate the solution since it cannot resolve small subtle changes in faulting geometry, even on an ocean transform fault. In contrast, the non-fixed models are relatively robust against the model-plane geometry, and a similar slip evolution is obtained in all the models.

S6 Teleseismic inversion synthetic test with forward-modelled waveforms

We performed a synthetic test of the teleseismic inversion. Synthetic waveforms were generated by using the slip distribution of the optimum model. We added the Gaussian noise with zero mean and 1% variance to the dataset, and then we inverted the synthetic waveforms to investigate whether we could retrieve the solution. As shown in **Figure S12**, the synthetic test properly retrieves the input model, although a slight change in the peak slip and the focal mechanism can be seen.

Supplementary Figures

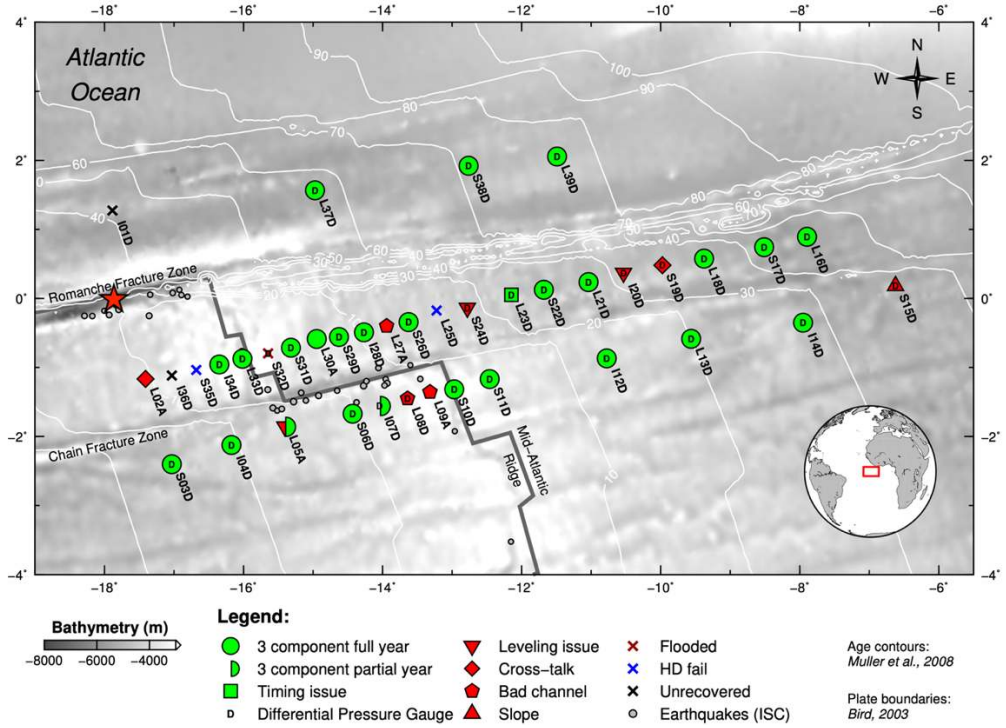

Figure S1: Full network map of the PI-LAB ocean-bottom seismometer deployment. All available stations were used for mainshock and aftershock sequence relocations. Stations are coloured according to instrument performance and data recovery. The red star gives the epicentre of the 2016 Romanche earthquake.

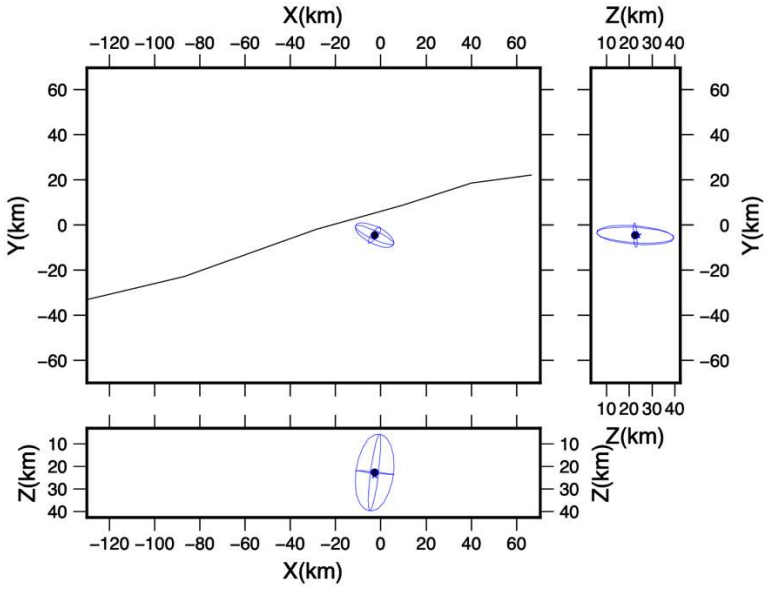

Figure S2: 68% confidence ellipsoid estimate for our relocated hypocentre of the Romanche earthquake projected in map view (top-left); the X-Z plane (bottom-left) and the Y-Z plane (top-right). The dot shows the Gaussian expected hypocentre and the star shows the maximum likelihood hypocentre estimate. The black line shows the approximate position of the Romanche Fracture Zone.

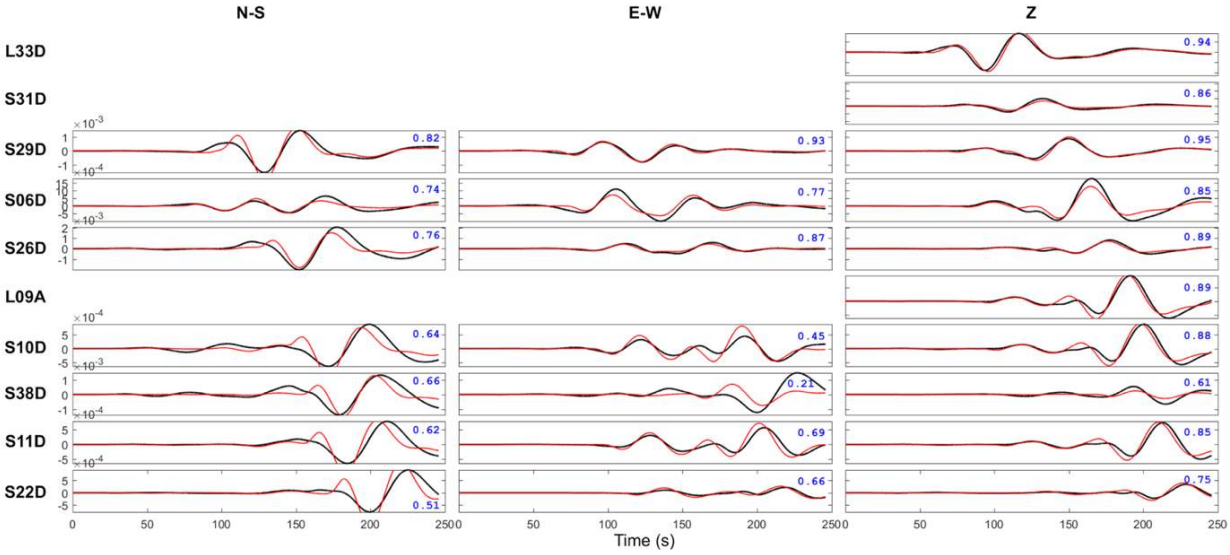

Figure S3: Fits between observed (black lines) and synthetic displacement waveforms (red lines) for the optimum single source low-frequency regional moment tensor of the Romanche earthquake. Waveforms are bandpass filtered between 100 s and 33 s period. Station labels are on the left; component labels along the top. Blue numbers show the variance reduction for each component.

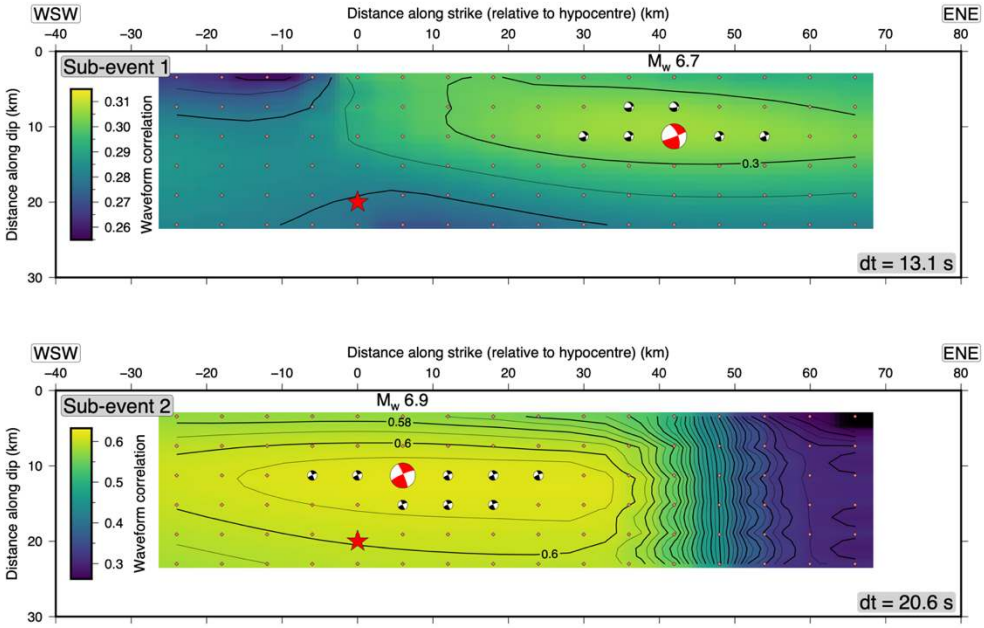

Figure S4: Waveform correlation as a function of trial-point-source position along the fault plane for Sub-Event 1 (SE1; top) and Sub-Event 2 (SE2; bottom). The hypocentre position is given as the red star. The best-fitting regional moment tensor and centroid position is given by the red beach ball. Black beach balls show solutions that have a waveform correlation within 5% of the optimum solution. Diamonds show the location of trial point-sources.

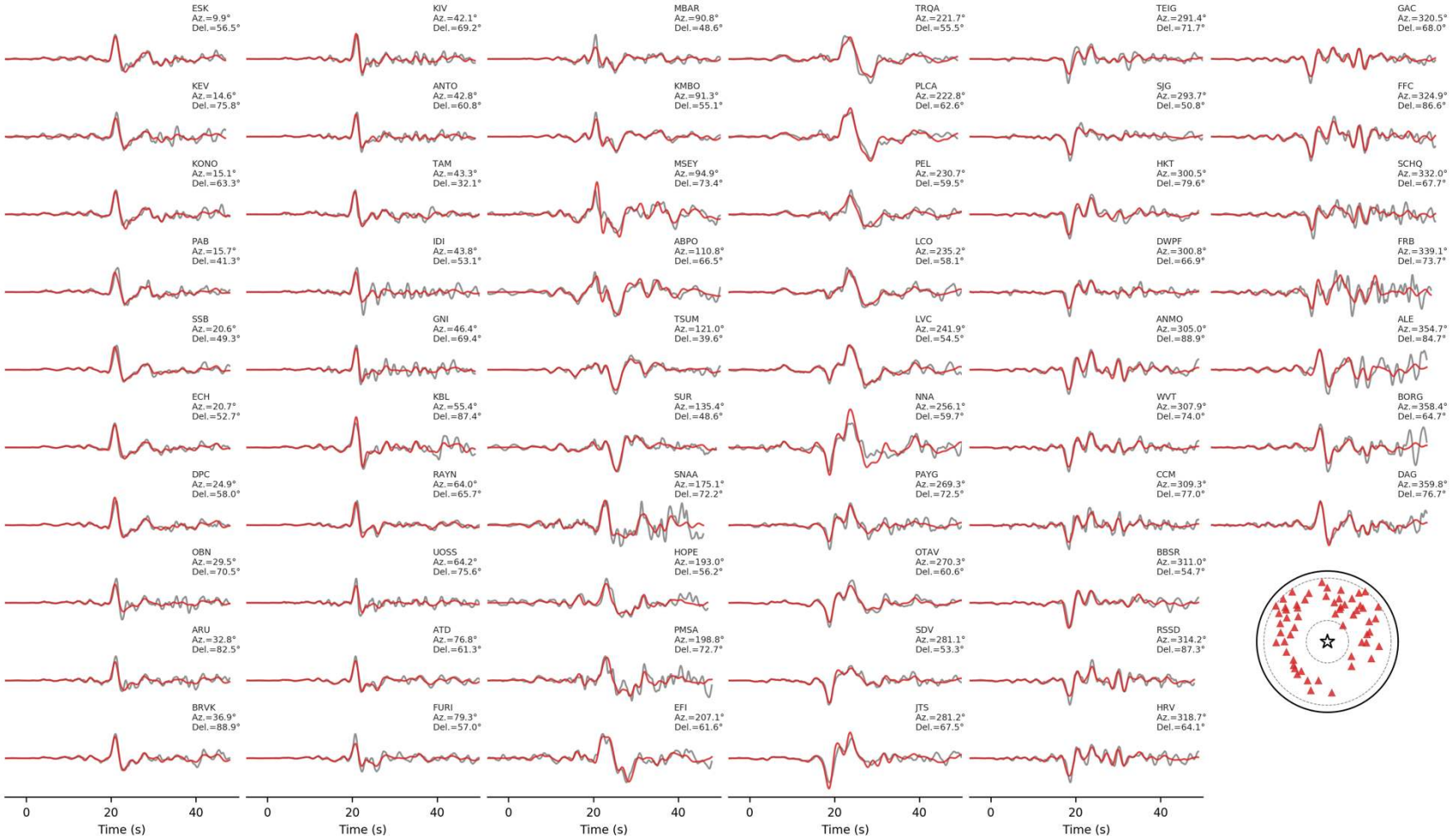

Figure S5: Observed P-waveforms (grey) and synthetic fits (red) for our preferred teleseismic slip model. The right-bottom panel is the station distribution. The star and triangles correspond to the epicentre and stations, respectively. Dashed lines are epicentral distances at 30° and 90°.

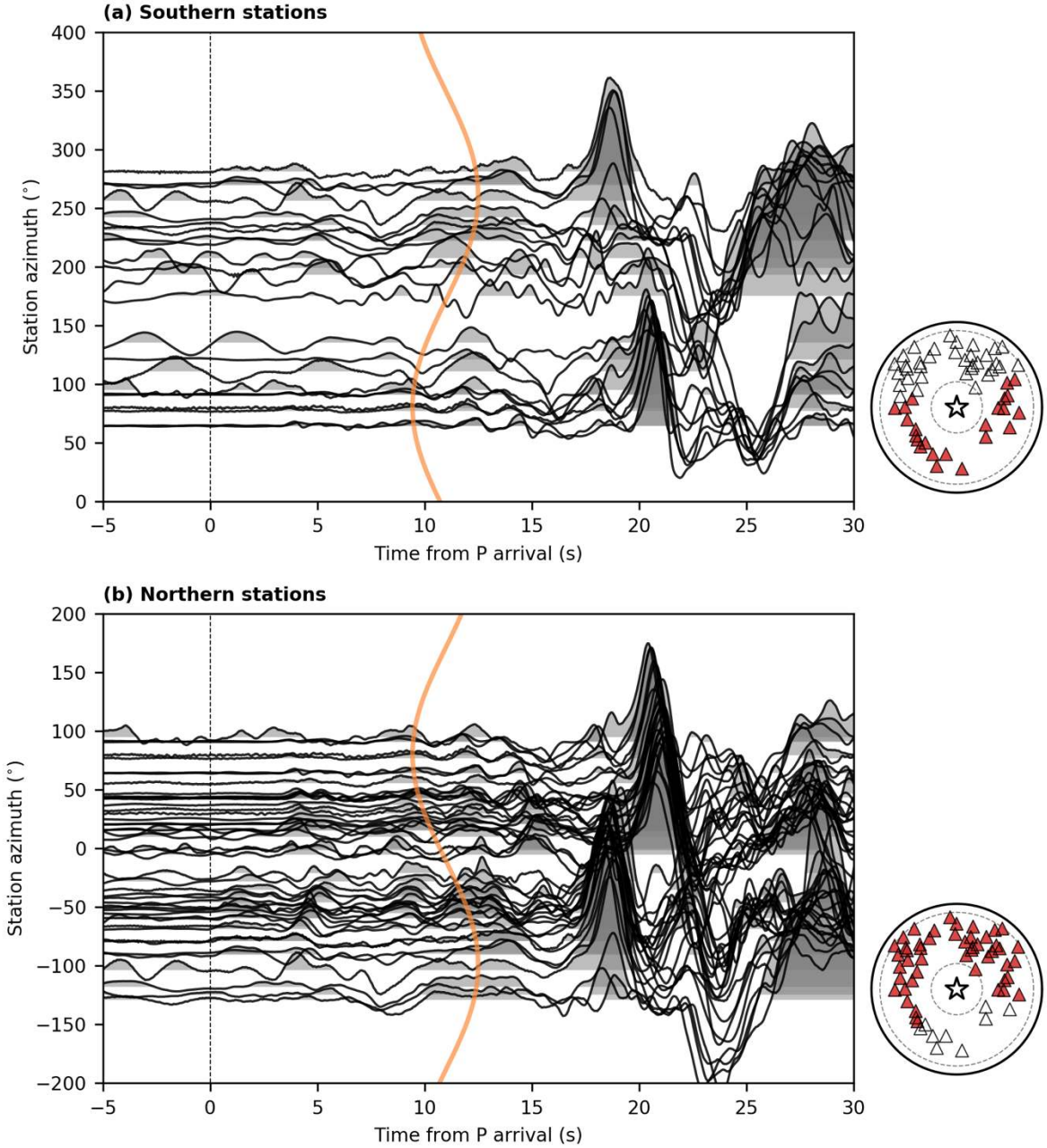

Figure S6: Raw P-wave velocity waveforms plotted versus azimuth. The traces are aligned by P-wave arrival with polarity flipped, and each trace is normalized by its maximum amplitude. Vertical curve is an expected rupture duration[10,11] of SE1, assuming rupture length for 32.9 km toward 80.4° azimuth from the epicentre with rupture speed at 3 km/s. The averaged apparent velocity was assumed to be 21.5 km/s calculated with TauP Toolkit[11]. The inset shows the station distribution. Red triangles are stations shown in each panel. The white star is the epicentre. Dashed circles are epicentral distances at 60° and 90°.

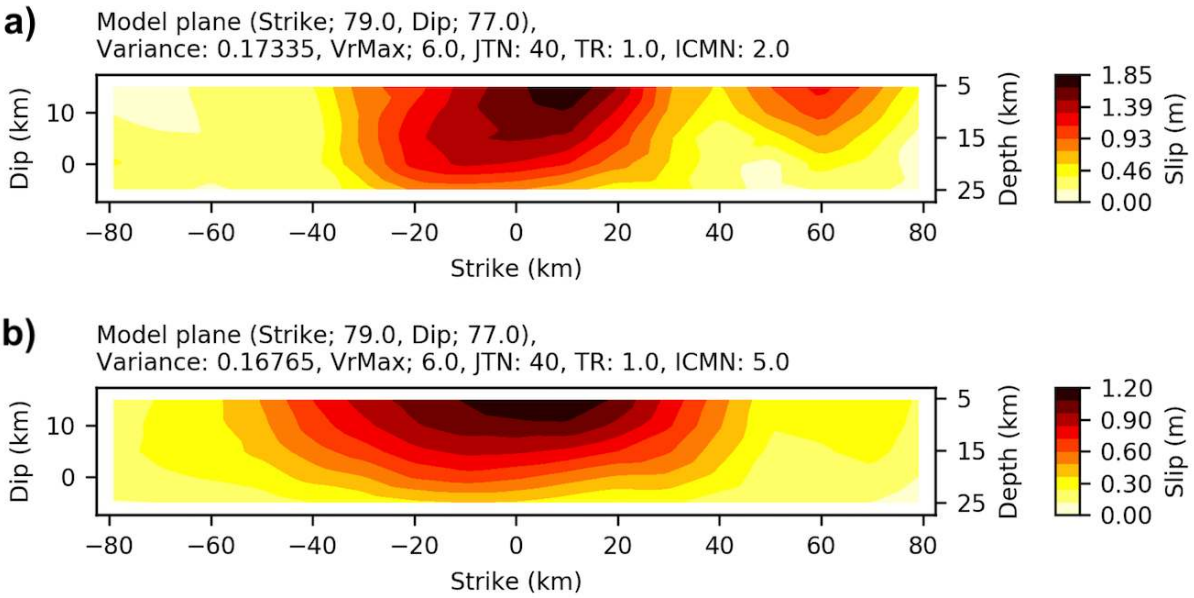

Figure S7: Comparison of the time-integrated slip model between inversions (a) in which the double-couple mechanism of each sub-fault is pre-determined by the model geometry; and (b) in which each sub-fault's double-couple mechanism is allowed to vary. Parameters above each panel are as follows: strike and Dip are the geometry of the model plane; variance shows the fit between observed and synthetic waveforms; VrMax is an assumption of maximum rupture velocity that determines the edge of model space where the following slip is represented; JTN is a number of B-spline that forms slip-rate function (if TR is 1.0, then the duration of slip-rate function is 40 s); TR is the time interval (sec) of slip-rate function; ICMN is a flag of model flexibility: if 2.0, the slip is represented as two-basis double couple components (fixed model), and if 5.0, the slip is represented by five-basis double couple components (non-fixed model).

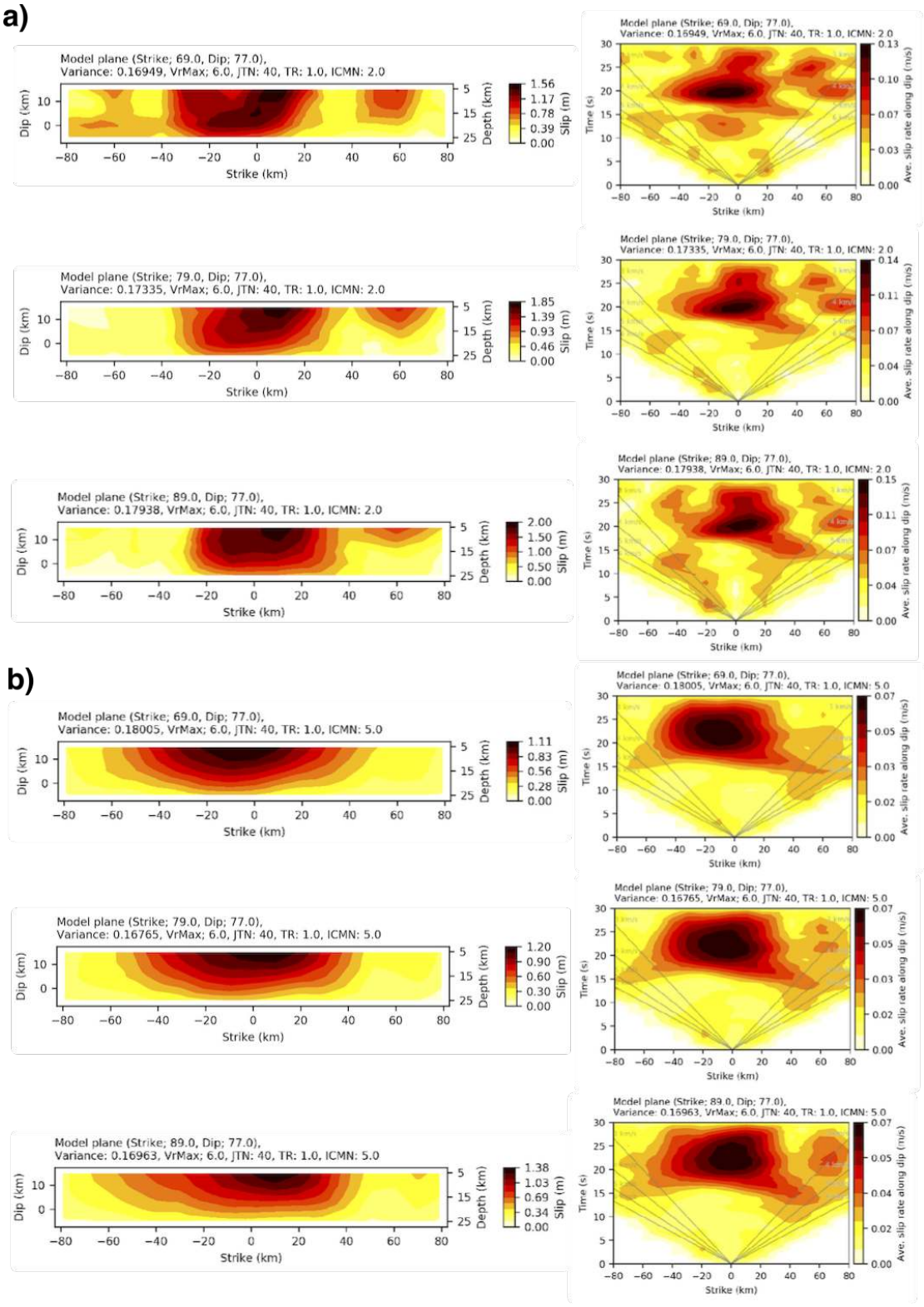

Figure S8: Effect of varying fault strike angle by ±10° for a) assuming slip vectors equal to the prescribed fault plane, and b) using flexible slip vectors. The panels on the left show the time-integrated slip distribution; the panels on the right show the slip-rate evolution as a function of distance along strike and time. The assumed fault geometry is given in the text above each panel.

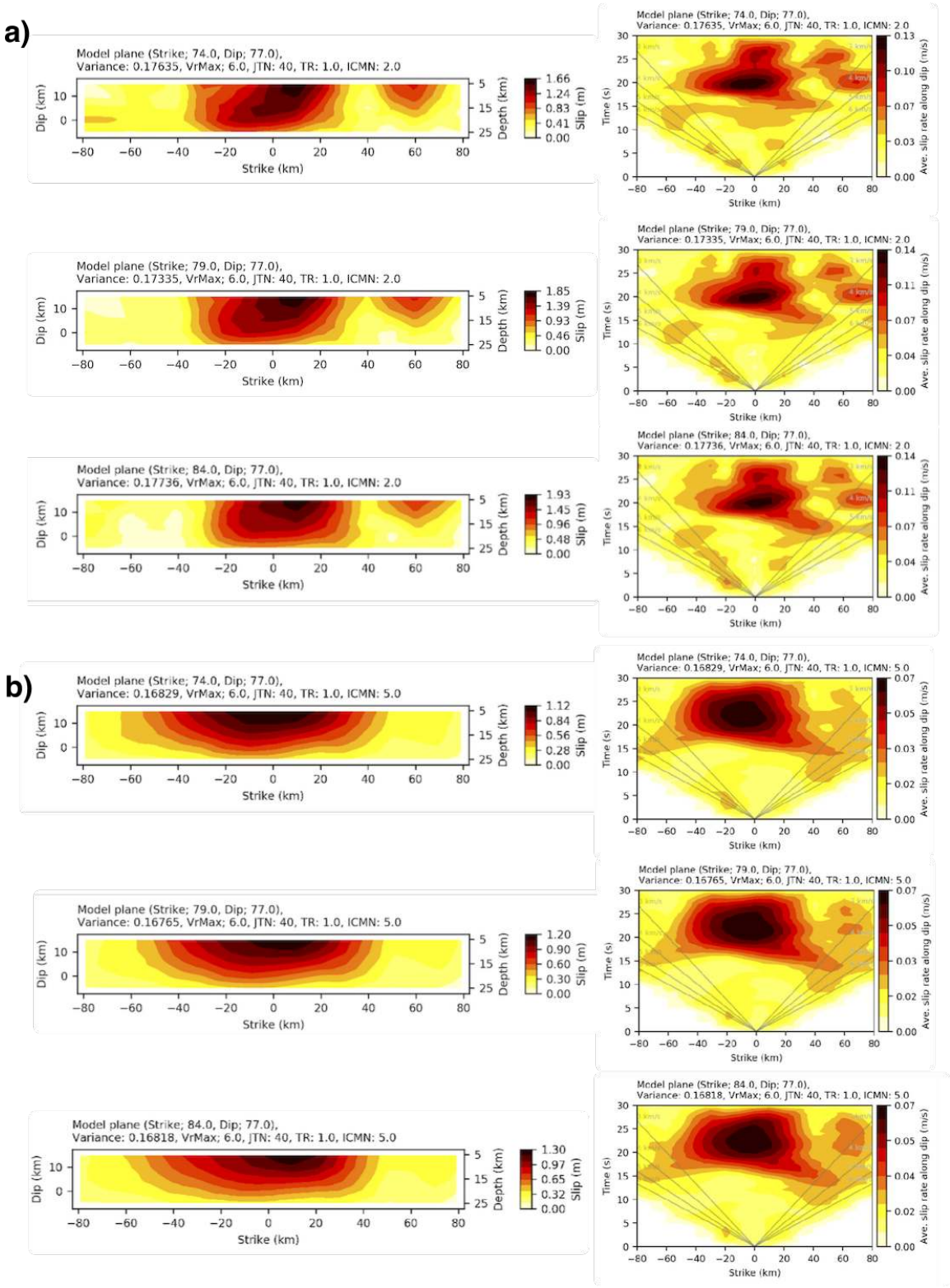

Figure S9: Effect of varying fault strike angle by ±5° for a) assuming slip vectors equal to the prescribed fault plane, and b) using flexible slip vectors. The panels on the left show the time-integrated slip distribution; the panels on the right show the slip-rate evolution as a function of distance along strike and time. The assumed fault geometry is given in the text above each panel.

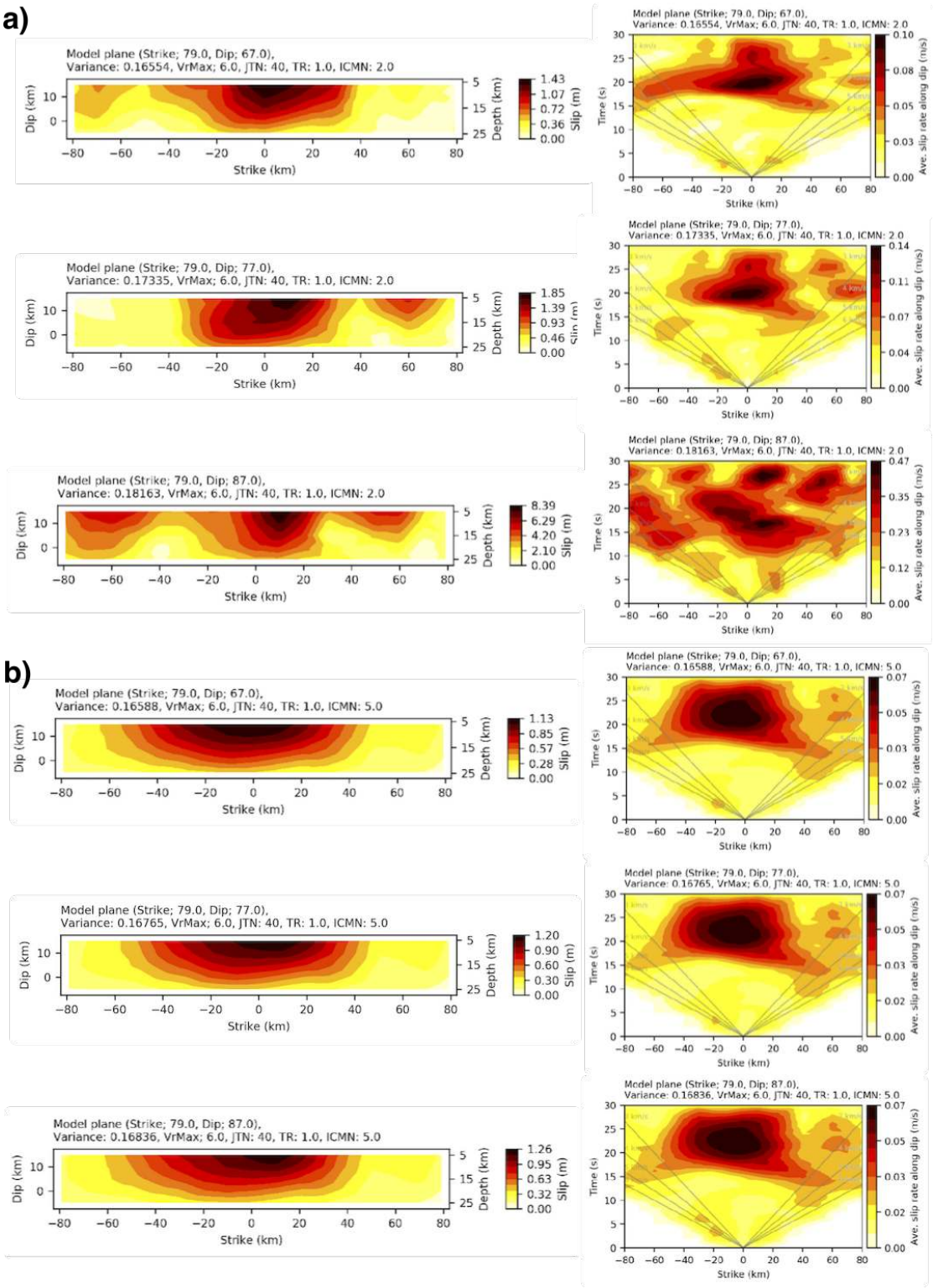

Figure S10: Effect of varying fault dip angle by ±10° for a) assuming slip vectors equal to the prescribed fault plane, and b) using flexible slip vectors. The panels on the left show the time-integrated slip distribution; the panels on the right show the slip-rate evolution as a function of distance along strike and time. The assumed fault geometry is given in the text above each panel.

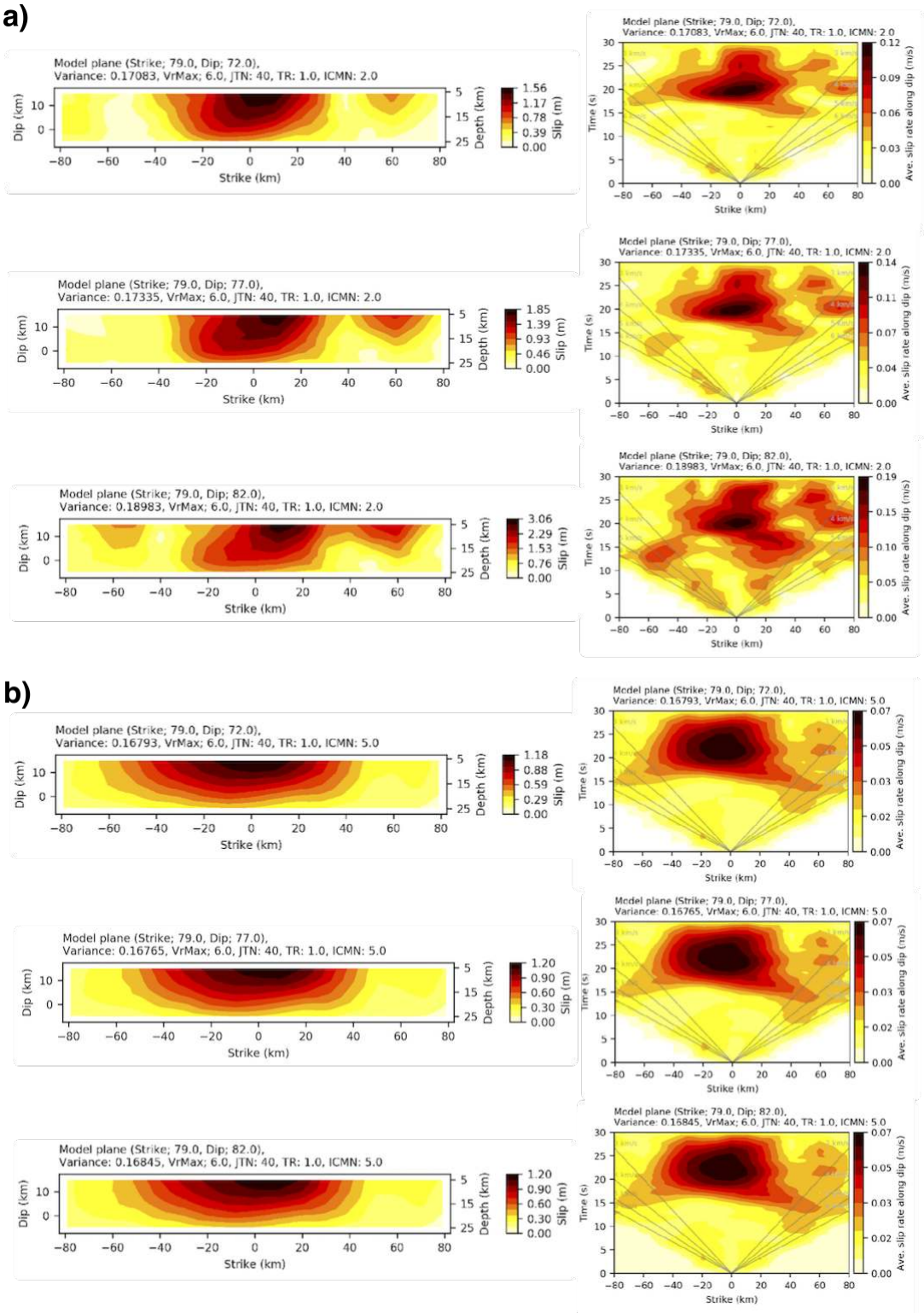

Figure S11: Effect of varying fault dip angle by ±5° for a) assuming slip vectors equal to the prescribed fault plane, and b) using flexible slip vectors. The panels on the left show the time-integrated slip distribution; the panels on the right show the slip-rate evolution as a function of distance along strike and time. The assumed fault geometry is given in the text above each panel.

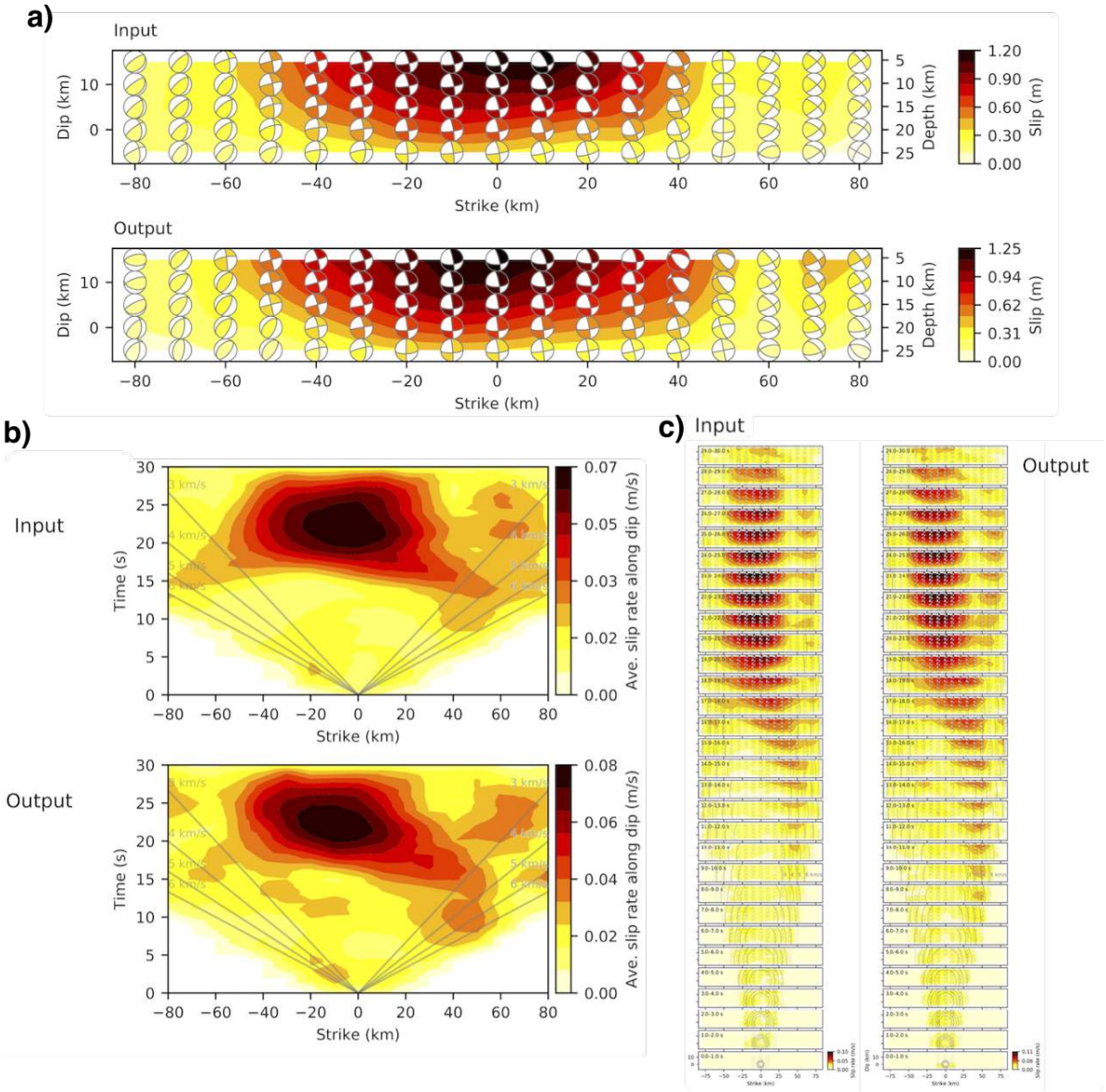

Figure S12: Synthetic test using our optimum teleseismic slip model for the Romanche earthquake as input. a) Time-integrated slip model; b) evolution of slip rate over time and distance along the fault; c) time snapshots showing the 2-D evolution of slip rate.

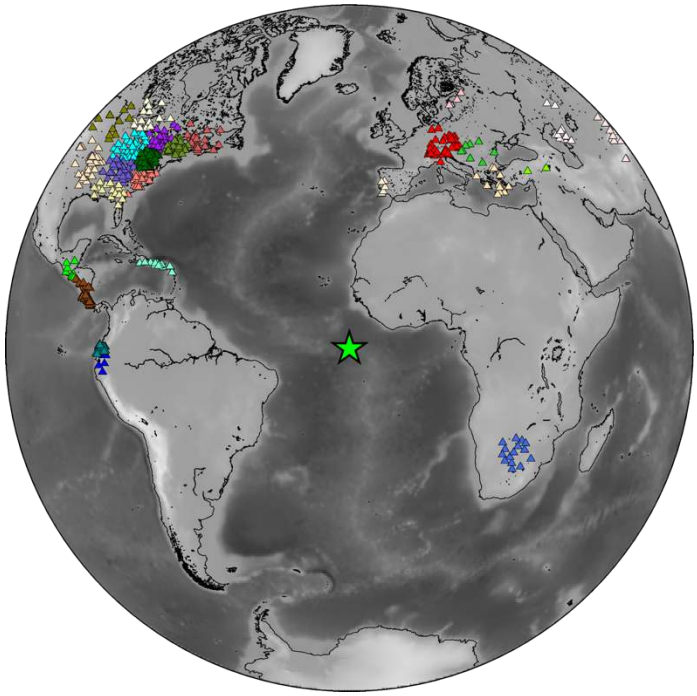

Figure S13: Locations of stations (triangles) in sub-arrays used for the teleseismic back-projection imaging. Each sub-array has been assigned a unique colour. The green star shows the epicentre of the Romanche mainshock.

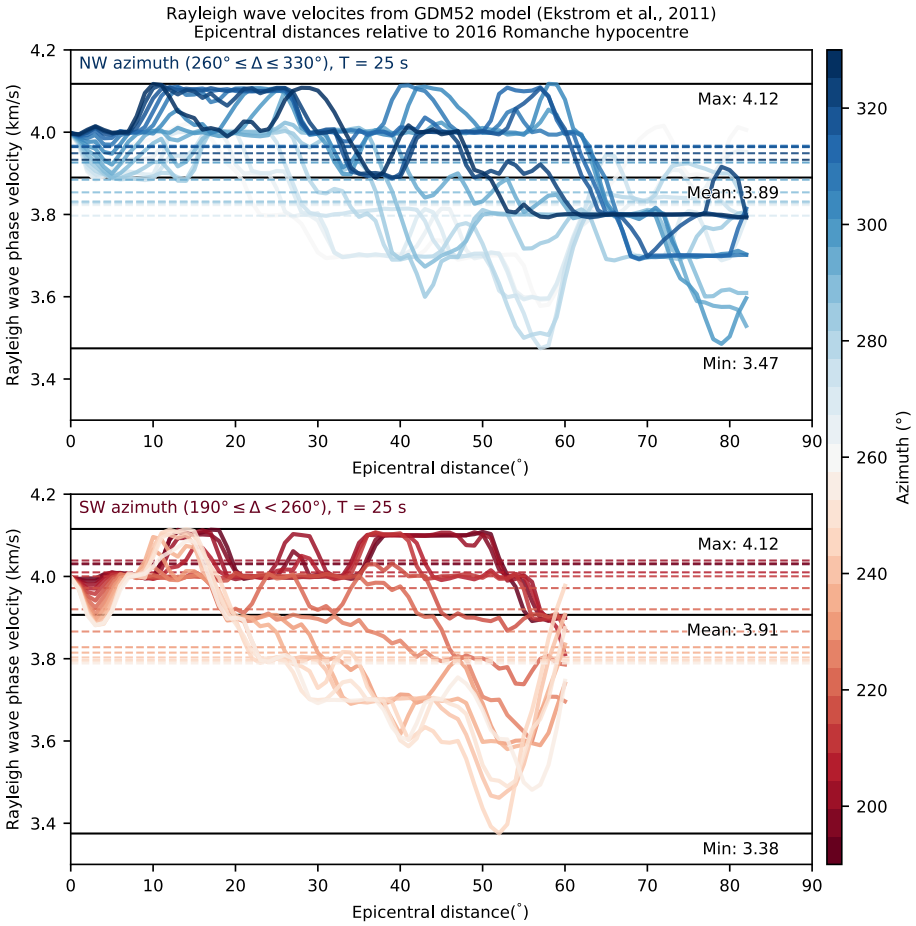

Figure S14: Predicted Rayleigh wave phase velocities along source-station paths for north-westerly azimuths (top) and south-westerly azimuths (bottom) at periods of 25 s from the GDM52 model[12].

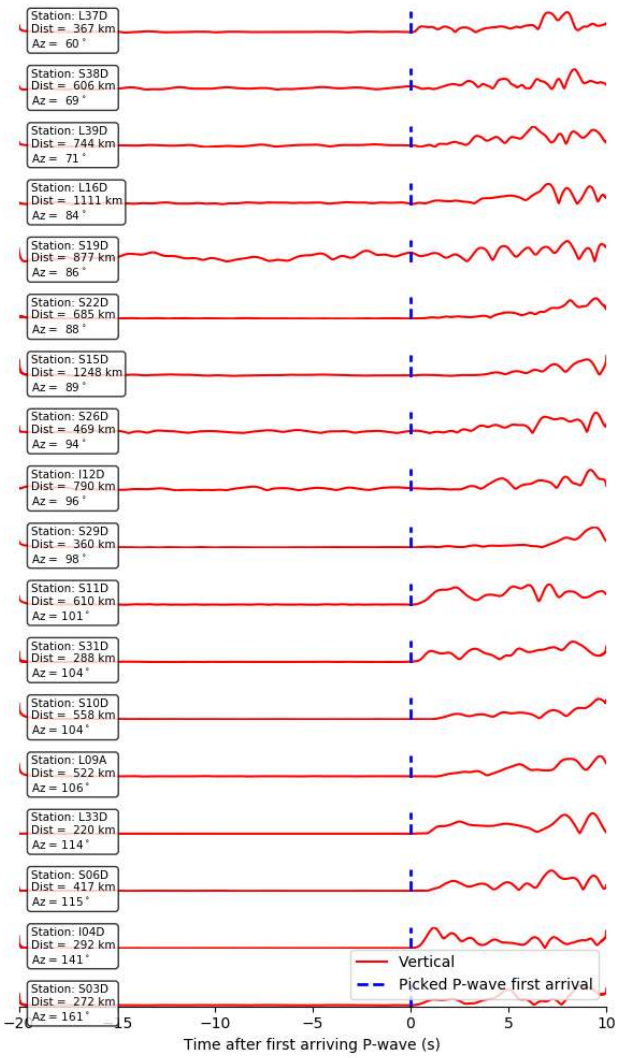

Figure S15: Velocity waveform envelopes bandpass filtered between 0.4 and 1.5 Hz showing the first 10 s of seismic radiation from the Romanche rupture. Waveforms are aligned to the first picked P-wave arrival.

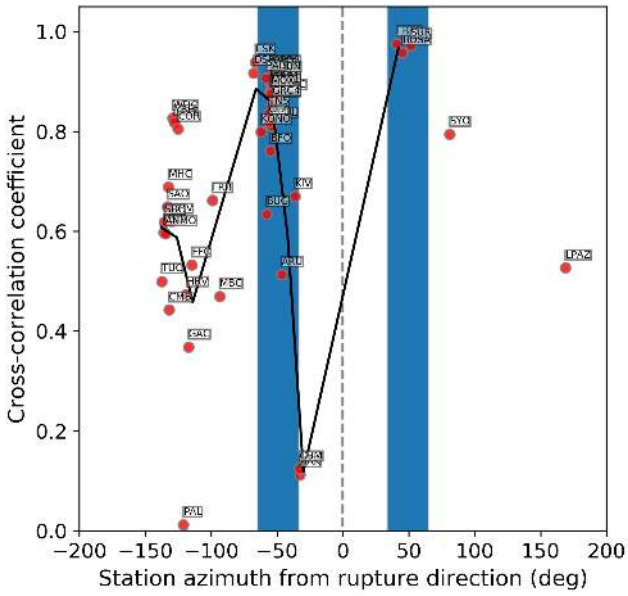

Figure S16: Rayleigh wave cross-correlation values for the 1994 M_w 7.1 Romanche earthquake and a co-located M_w 6.3 earthquake on 1996-11-28.

Supplementary tables

Table S1: Hypocentre estimates for the Romanche mainshock

Hypocentre source / reporting agency	**Latitude**	**Longitude**	**Depth (km)**	**Horizontal distance to our optimum epicentre (km)**
This study (using phase arrivals on OBSs)	0.092°S	17.830°W	23	-
NEIC-USGS	0.046°S	17.826°W	10	3.1
ISC-EHB	0.085°S	17.788°W	10	6.1
GFZ-GEOFON	0.060°S	17.780°W	17	6.9
GEOSCOPE (IPGP)	0.072°S	17.814°W	16	3.0

Table S2: Double-couple percentages from different single-source CMT estimates.

Source	**Double-couple percentage**
This study (low frequency single-point source CMT)	98.7%
GFZ-GEOFON	99.7%
GCMT	77.9%
USGS-NEIC	76.9%

References

1. Doran, A. K. & Laske, G. Ocean-Bottom Seismometer Instrument Orientations via Automated Rayleigh-Wave Arrival-Angle Measurements. *B. Seismol. Soc. Am.* **107**, 691 708 (2017).

2. Agius, M., Harmon, N., Rychert, C., Tharimena, S. & Kendall, J. -M. Sediment Characterization at the Equatorial Mid-Atlantic Ridge From P-to-S Teleseismic Phase Conversions Recorded on the PI-LAB Experiment. *Geophys. Res. Lett.* **45**, 12,244-12,252 (2018).

3. Hicks, S. P., Rietbrock, A., Ryder, I. M., Lee, C.-S. & Miller, M. Anatomy of a megathrust: The 2010 M8.8 Maule, Chile earthquake rupture zone imaged using seismic tomography. *Earth. Planet. Sci. Lett.* **405**, 142 155 (2014).

4. Lomax, A., Michelini, A. & Curtis, A. Earthquake location, Direct, Global-search Methods. *Encyclopedia of complexity and systems science* 2449 2473 (2009) doi:10.1007/978-0-387-30440-3_150 .

5. Roessler, D. *et al.* Cluster-search based monitoring of local earthquakes in SeisComP3. *AGU Fall Meeting Abstracts* (2016).

6. Myers, S. C., Johannesson, G. & Hanley, W. A Bayesian hierarchical method for multiple-event seismic location. *Geophys. J. Int.* **171**, 1049 1063 (2007).

7. Bakun, W. H. & Joyner, W. B. The ML scale in central California. *Science* **74**, 1827 1843 (1984).

8. Sokos, E. N. *et al.* Asperity break after 12 years: The Mw6.4 2015 Lefkada (Greece) earthquake. *Geophys. Res. Lett.* **43**, 6137 6145 (2016).

9. Yagi, Y. & Fukahata, Y. Introduction of uncertainty of Green's function into waveform inversion for seismic source processes. *Geophys. J. Int.* **186**, 711 720 (2011).

10. Ammon, C. J. *et al.* Rupture process of the 2004 Sumatra-Andaman earthquake. *Science* **308**, 1133 1139 (2005).

11. Fan, W. & Shearer, P. M. Detailed rupture imaging of the 25 April 2015 Nepal earthquake using teleseismic P waves. *Geophys. Res. Lett.* **42**, 5744–5752 (2015).

12. Ekström, G. A global model of Love and Rayleigh surface wave dispersion and anisotropy, 25–250 s. *Geophys. J. Int.* **187**, 1668–1686 (2011).